OCCASION

This publication has been made available to the public on the occasion of the 50th anniversary of the United Nations Industrial Development Organisation.

DISCLAIMER

This document has been produced without formal United Nations editing. The designations employed and the presentation of the material in this document do not imply the expression of any opinion whatsoever on the part of the Secretariat of the United Nations Industrial Development Organization (UNIDO) concerning the legal status of any country, territory, city or area or of its authorities, or concerning the delimitation of its frontiers or boundaries, or its economic system or degree of development. Designations such as "developed", "industrialized" and "developing" are intended for statistical convenience and do not necessarily express a judgment about the stage reached by a particular country or area in the development process. Mention of firm names or commercial products does not constitute an endorsement by UNIDO.

FAIR USE POLICY

Any part of this publication may be quoted and referenced for educational and research purposes without additional permission from UNIDO. However, those who make use of quoting and referencing this publication are requested to follow the Fair Use Policy of giving due credit to UNIDO.

CONTACT

Please contact publications@unido.org for further information concerning UNIDO publications.

For more information about UNIDO, please visit us at www.unido.org

UNITED NATIONS INDUSTRIAL DEVELOPMENT ORGANIZATION
Vienna International Centre, P.O. Box 300, 1400 Vienna, Austria
Tel: (+43-1) 26026-0 · www.unido.org · unido@unido.org

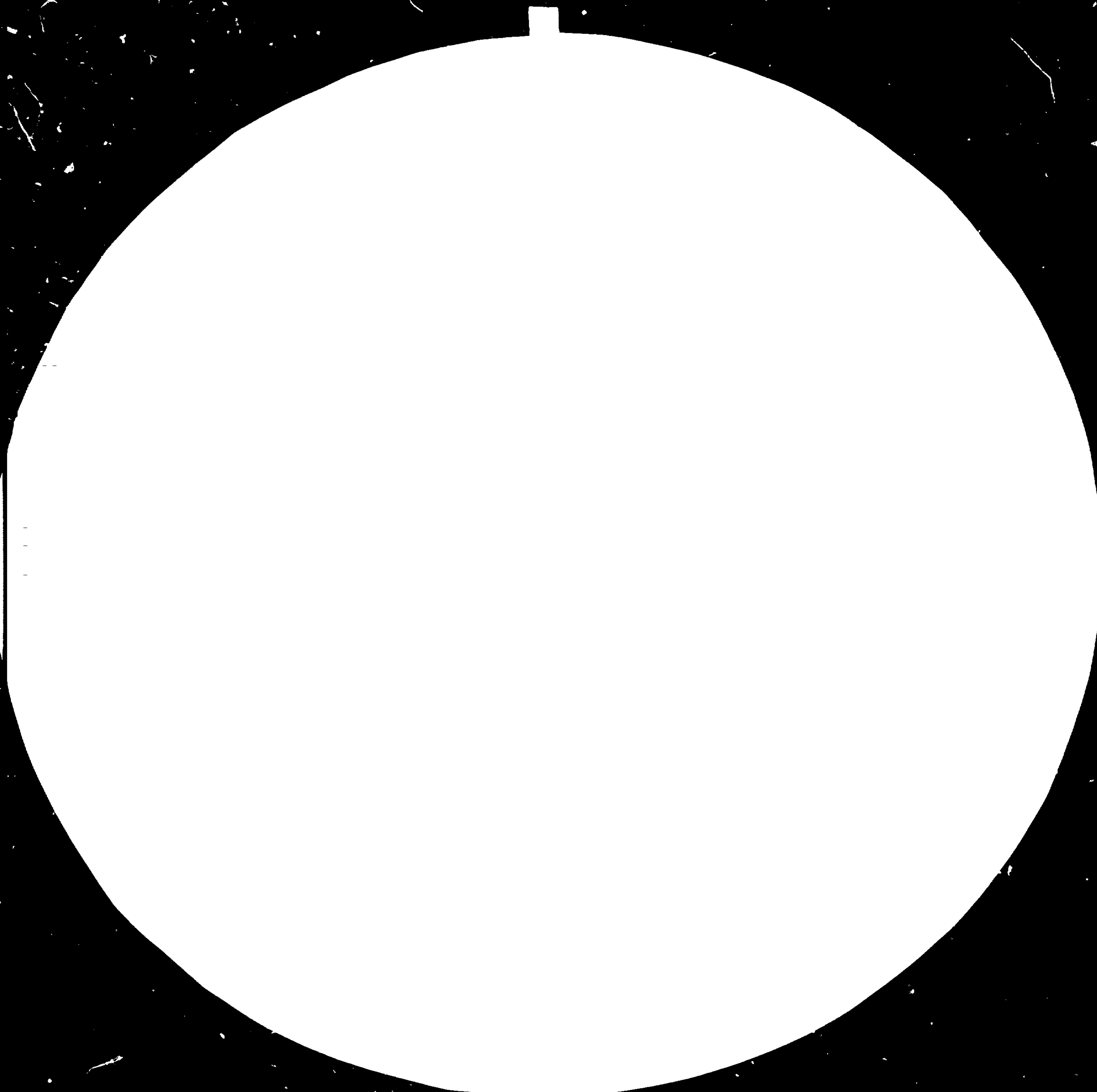

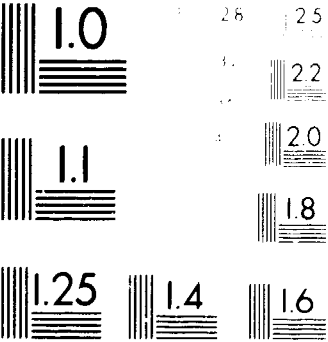

MICROCOPY RESOLUTION TEST CHART

NATIONAL BUREAU OF STANDARDS
STANDARD REFERENCE MATERIAL 1010a
(ANSI and ISO TEST CHART No. 2)

UNITED NATIONS INDUSTRIAL DEVELOPMENT ORGANISATION

14342

REPORT

by

J.L. WHITE

DP/MEX/78/017

Mexico. "Plasticos en la Agricultura".

1984

INTRODUCTION

In response to the inquiry from UNIDO, the author travelled to Saltillo, Mexico, on April 15, 1984. He remained based there at the Centro de Investigacion Quimica Applicada (CIQA) until Thursday, April 26, when he travelled to Mexico City. He departed from Mexico City to the U.S.A. on Sunday, April 29.

The ext section of the report will deal with activities at CIQA in Saltillo.

REPORT

The primary activities at CIQA involved (i) lectures, (ii) consultation on individual problems. The major lectures were given on Tuesday, April 17 and Wednesday, April 18, on the manufacture and properties of film. The first lecture emphasized the dynamics of manufacture of tubular film with some discussion of multiple layer film. The second lecture largely dealt with the structure and properties of films. Special attention was given to structure-processing relationships in fabricated film.

The general contents of the lectures on film extrusion followed the outlines of experimental studies worked out in the authors'-laboratories. The contents of the first lecture are contained in

T. Kanai and J.L. White, "Kinematics, Dynamics and Stability of the Tubular Film Extrusion of Various Polyethylenes"
Polym Eng Sci 24, 1185 (1984)

This is enclosed in Appendix A.

The materials in the second lecture followed the contents of two papers,

K.J. Choi, J.E. Spruieil and J.L. White, "Orientation and Morphology of High-Density Polyethylene Film Produced by the Tubular Blowing Method and its Relationship to Process Conditions"
J Polym Sci Polym Phys 20, 27-47, (1982)

and

H. Ashizawa, J.E. Spruiell and J.L. White, "An Investigation of Optical Clarity and Crystalline Orientation in Polyethylene Tubular Film"
Polym Eng Sci 24, 1035 (1984)

These are included in Appendices B and C.

Various problems related to film for agricultural purposes were considered in individual discussions. These included (i) the light scattering and absorbence characteristics of single and multiple layer films, (ii) the rheological and melt processing behavior of polymer blends being fabricated into films.

The discussions related to light penetrating through films involved eliminating parts of the electrimagnetic spectrum of radiation by controlling the refractive indices and absorbing characteristics of the individual polymer layers. These could be influenced by dyes, pigments and other additives to the polymers prior to co-extrusion. This was deemed possible and further study was considered. Improvements in melt processability through blending of different polymers was considered. Generally incompatible polymers would be used and phase morphology characteristics would be complicated. The influence of such blending or light scattering characteristics would need considerable study.

Other problems also received attention during this stay. These included the characteristics and potentials of (i) guayule rubber developed in northern Mexico, (ii) Mexican hevea rubber.

The possibility of developing a rubber research development organization in Mexico equivalent to that in Malaysia was discussed. This would treat both hevea and guayule. The purpose would be to greatly stimulate the production and upgrade the quality of naturally occuring cis-1,4 polyisoprenes produced in Mexico. This production would first satisfy the domestic market and then become a significant export to North America.

Appendix A

Kinematics, Dynamics and Stability of the Tubular Film Extrusion of Various Polyethylenes

TOSHITAKA KANAI* *and* JAMES L. WHITE†

Polymer Engineering
University of Tennessee
Knoxville, TN 37996

A basic study of the kinematics, dynamics, and heat transfer occuring during tubular film extrusion of polyethylene is outlined. Three rheologically characterized polyethylenes, a low-density polyethylene (LDPE), a linear-low-density polyethylene (L-LDPE), and a high-density polyethylene (HDPE) were used in this study. The kinematics and stability of the tubular film process were investigated over a wide range of blow-up ratios, drawdown ratios, and frost-line heights. Local deformation rates along the bubble have been determined. Regions of stability and instability are described. Tensions and inflation pressures have been measured and expressed in terms of local elongational viscosities. Temperature profiles along the bubble were determined and interpreted in terms of local heat transfer coefficients. Positions of crystallization and temperature profiles have been noted and used to estimate rates of crystallization. The characteristics of the LDPE, LLDPE, and HDPE are contrasted.

INTRODUCTION

There is no polymer-processing operation more important than tubular film extrusion. There have been, however, few basic experimental studies of this operation (1–11). Menges and Predohl (1) and Ast (2, 3) have considered heat transfer from the film to the surroundings. Farber and Dealy (4), Han and Park (5) and Winter (6) have studied kinematics and the latter dynamics. In a second series of experiments, Han, *et al.* (7) studied the occurrence of bubble instabilities. Maddams and Preedy (8) and investigations in our laboratories (9–11) have considered the development of orientation and crystalline morphology in tubular film extrusion. One obtains a very incomplete picture from these studies. The relative stability of different melts over a range of operating conditions is not clear. There are really no broad vertically integrated experimental studies of the tubular film extrusion of polymer melts.

In the present paper, we describe a comparative study of the kinematics, bubble stability, and dynamics of a series of polyethylenes, specifically a low-density polyethylene (LDPE), a linear-low-density polyethylene (LLDPE), and a high-density polyethylene (HDPE). The HDPE is primarily a linear homopolymer, while the LLDPE is a linear copolymer in which small amounts of the second monomer breakup some of the ethylene crystallinity. The LDPE is a long-chain branched polymer, with the branching being introduced by the free radical mechanism of the polymerization.

BACKGROUND

Kinematics

The kinematics of tubular film extrusion first received attention by Pearson (12) and later in more detail in a series of papers by Pearson and Petrie (13–15). If we take "1" as the machine direction, "2" as the circumferential direction and "3" as the thickness direction in a local cartesian coordinate frame, we may write for the deformation rate tensor:

$$d_{11} = \frac{\partial v_1}{\partial \xi_1} = \frac{Q\cos\theta}{2\pi RH}\left(-\frac{1}{H}\frac{dH}{dz} - \frac{1}{R}\frac{dR}{dz}\right) \qquad (1a)$$

$$d_{22} = \frac{\partial v_2}{\partial \xi_2} = \frac{Q\cos\theta}{2\pi RH}\frac{1}{R}\frac{dR}{dz} \qquad (1b)$$

$$d_{33} = \frac{\partial v_3}{\partial \xi_3} = \frac{Q\cos\theta}{2\pi RH}\frac{1}{H}\frac{dH}{dz} \qquad (1c)$$

where Q is the extrusion rate, R is the bubble radius at any elevation z, and θ is the angle between the axis of the bubble and a tangent to the surface of the bubble. The derivative of *Eq 1a* involves an assumption of constant density which is not quite fully satisfied because of cooling and crystallization.

We may represent special kinematic cases (9). For uniaxial extension this leads to

---

* Present Address: Idemitsu Petrochemical Co., Ltd., 1660 Kamiizumi Sodegaura-[illegible] Chiba, Japan.

† Present Address: Polymer Engineering Center, University of Akron, Akron, Ohio [illegible]

$$d_{33} = d_{22}, \qquad \frac{\partial v_3}{\partial \xi_3} = \frac{\partial v_2}{\partial \xi_2} \qquad (2a)$$

$$\frac{1}{R}\frac{dR}{dz} = \frac{1}{H}\frac{dH}{dz} \qquad (2b)$$

If uniaxial kinematics are maintained along the length of the bubble, Eq 2b may be integrated to give

$$\frac{v_L}{v_0} = \frac{1}{B^2} \qquad (3)$$

where L represents the takeup and 0 the die exit. B is the blowup ratio R_L/R_0.

For planar extension

$$d_{33} = 0, \qquad \frac{\partial v_3}{\partial \xi_3} = 0 \qquad (4a)$$

$$\frac{1}{R}\frac{dR}{dz} = 0 \qquad (4b)$$

If this is maintained along the length of the bubble, we have

$$B = 1, \qquad \frac{v_L}{v_0} = \frac{H_0}{H_L} \qquad (5a,b)$$

For equal biaxial extension in the bubble

$$d_{11} = d_{33}, \qquad \frac{\partial v_1}{\partial \xi_1} = \frac{\partial v_3}{\partial \xi_3} \qquad (6a)$$

$$-\frac{1}{H}\frac{dH}{dz} - \frac{1}{R}\frac{dR}{dz} = \frac{1}{R}\frac{dR}{dz} \qquad (6b)$$

If this is maintained along the length of the bubble, Eq 6b leads to

$$\frac{v_L}{v_0} = B \qquad (7)$$

The drawdown ratio is equal to the blowup ratio.

We have sought to roughly specify the kinematics of bubbles in terms of drawdown ratio v_L/v_0, blowup ratio B, and frost line height, z_F. The values of v_L/v_0 and B specify the biaxiality of the kinematics. These numbers coupled with the frost line height approximate the rates of deformation.

Dynamics

The force balance on tubular film is most readily developed from membrane theory as has been discussed by Alfrey (16). The first explicit derivation and discussion was in a series of papers by Pearson and Petrie (13–15) who show that it simplifies to the expressions

$$F = 2\pi R H \sigma_{11} \cos\theta + \pi \Delta p (R_L^2 - R^2) \qquad (8)$$

$$\Delta p = \frac{H\sigma_{11}}{R_1} + \frac{H\sigma_{33}}{R_2} \qquad (9)$$

$$R_1 = \frac{R}{\cos\theta}, \qquad R_2 = -\sec^3\theta \Big/ \frac{d^2R}{dz^2}$$

where σ_{11} is the stress in the machine direction, σ_{33} the stress in the circumferential direction, F is the drawdown force, Δp the bubble pressure and R_1 and R_2, the principal radii of curvature of the film.

Heat Balance

Consider an annular film emerging from a die and inflating to form a continuous bubble. The temperature decreases continuously along the machine direction. A differential heat balance over a vertical segment dz leads to the form

$$\rho c Q \cos\theta \frac{dT}{dz} = -2\pi R \{h(T - T_c) + \epsilon\sigma(T^4 - T_0^4)\} + Q \Delta H_f \cos\theta \frac{dX}{dz} \qquad (10)$$

where T is the mean temperature of the film, T_0 the temperature of the surroundings, T_c the cooling air temperature, h the local heat transfer coefficient, ϵ the relative emissivity, σ the Stefan-Boltzmann constant, ΔH_f the heat of fusion (crystallization), and X the fraction of crystallinity. Heat balances of this type, without the heat of crystallization are discussed by Petrie (17), Han and Park (18), and Wagner (19).

EXPERIMENTAL

Materials

Three different polyethylenes were included in this study. These are a traditional low density polyethylene (LDPE), a linear low density polyethylene (LLDPE), and a high density polyethylene (HDPE). The LDPE and LLDPE were supplied by Union Carbide and the HDPE by Phillips Petroleum. Densities and melt indices of the three polyethylenes are summarized in *Table 1*.

Rheological Measurements

The shear viscosity η and principal normal stress difference N_1 of the three melts were measured in a Rheometrics Mechanical Spectrometer at 180°C. The shear stress was determined from the torque and the principal normal stress difference from the thrust pushing apart the cone and plate (20, 21). The uniaxial elongational flow characteristics of the filaments were investigated on an elongational rheometer developed in our laboratories (22, 24).

Tubular Film Extrusion

A ¾ inch Rainville screw extruder with an annular blown film die (inner diameter = 1.496 cm, outer

Table 1. Characterization of Polyethylene Samples

Polymer	Supplier	Density	Melt Index	$\eta_0 \times 10$[illegible] poise	M_n	M_w	M_w/M_n
LDPE	Union Carbide	0.923	1.9	1.9	27.2	110.[illegible]	[illegible]
LLDPE	Union Carbide	0.919	2.1	0.72	21.9	83.7	3.[illegible]
HDPE	Phillips Petroleum	0.9[illegible]	0.3	~6	12.0	173.2	14.[illegible]

diameter = 1.605 cm) was used in this study. Films were prepared with a range of drawdown ratios, v_L/v_0, blowup ratios, *B*, and frost-line heights z_F. The variables investigated are summarized in *Table 2*.

An 8mm motion picture projector was used to determine velocity profiles in the machine direction as well as bubble shape. The tension in the machine direction was obtained with a Tensitron Web Tensiometer. The pressure inside of the bubble was determined with a manometer.

The temperature profiles along the surface of the bubble were measured with an infrared pyrometer (Ircon CH-34), which involves no surface contact.

During tubular film extrusion, air is blown along the outside of the bubble to control the heat transfer rates with the surroundings (*Fig. 1*). This air velocity was measured with an air velocity meter (Thermo Systems, Inc. Model 1650 hot wire constant temperature anemometer).

RHEOLOGICAL MEASUREMENTS

Results

The shear viscosity function $\eta(\dot{\gamma})$ of the three melts at 180°C are shown in *Fig. 2*. The HDPE has the highest viscosity and the L-LDPE, the lowest. The zero shear viscosities, η_0, are summarized in *Table 1*. The viscosities $\eta(\gamma)$ are constant at low shear rate and decrease with increasing $\dot{\gamma}$.

The principal normal stress difference, N_1, of the three melts is plotted as a function of shear stress, τ_{12}, in *Fig. 3*. The data order with HDPE the largest and LLDPE the lowest.

The transient elongational viscosity, χ, of the filaments is plotted as a function of time for various elongation rates in *Fig. 4 a,b,c*. The LDPE and LLDPE achieve steady states but the HDPE does not, apparently failing by ductile necking at low total elongations. In *Fig. 5* we plot steady-state elongational viscosity, χ, as a function of *E* for the LDPE and LLDPE and the maximum achieved value χ_{max} for the HDPE. The LLDPE data is constant with a value near $3\eta_0$. The LDPE results are constant at low stretch rates (at a value about $3\eta_0$) and then increase at higher elongation rates. The χ_{max} of HDPE is a decreasing function of stretch rate, generally greater than $3\eta_0$.

Table 2. Range of Kinematic Conditions Investigated for Stable Bubbles

(Q = 0.75 kg/hr with stable operation)

Polymers	v_L/v_0	Film Thickness	Bubble Diameter	B	Frost-line Height z_F
LDPE	(−)	(μ)	(cm)	(−)	(cm)
	4	39.3	5.25	3.5	2.2
	4	39.3	5.25	3/5	6
	4	39.3	5.25	3.5	9
	4	39.3	5.25	3.5	12
	2	78.6	5.25	3.5	12
	8	19.7	5.25	3.5	12
LLDPE	4	39.3	5.25	3.5	2
	4	39.3	5.25	3.5	6
	4	39.3	5.25	3.5	9
	4	39.3	5.25	3.5	12
	2	78.6	5.25	3.5	12
	6	26.2	5.25	3.5	12
HDPE	4	39.3	5.25	3.5	2
	4	39.3	5.25	3.5	6
	4	39.3	5.25	3.5	9
	4	39.3	5.25	3.5	12
	2	79.6	5.25	3.5	12
	8	19.7	5.25	3.5	12

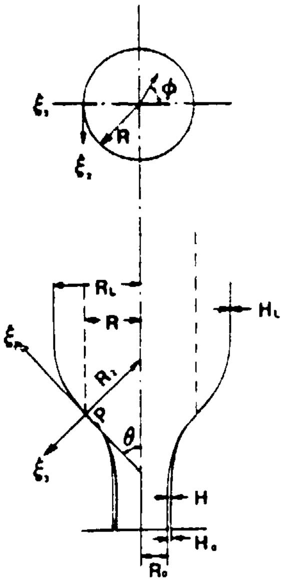

Fig. 1. Tubular film extrusion.

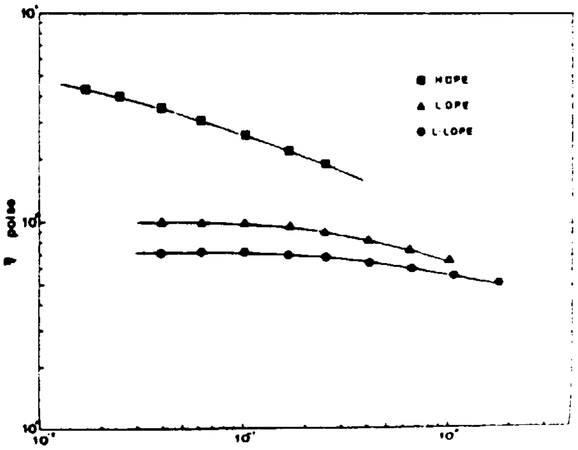

Fig. 2. Shear viscosity η-shear rate, γ, data for LDPE, LLDPE, and HDPE melts.

Discussion

In a study of tubular film extrusion, the elongational flow behavior should be of most interest. The elongational flow results described above are generally quite similar to those obtained by earlier investigators, most notably Ide and White (24). As described by these authors, molten LDPE filaments draws out in a stable manner while HDPE filaments develop necks and breaks short. Elongational viscosities were only determined for the former which were constant at low deformation rate where they equaled $3\eta_0$ and increased at higher stretch rates

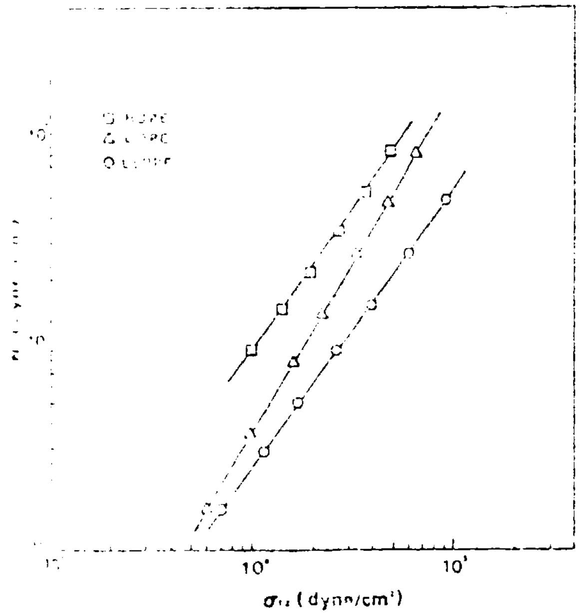

[illegible] normal stress difference N_1 as a function of [illegible] LDPE, LLDPE, and HDPE melts.

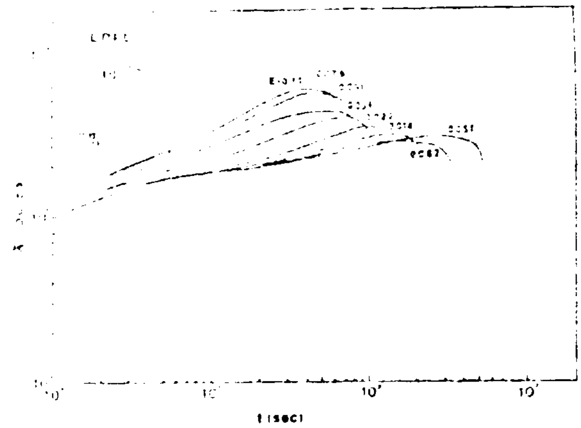

[illegible] elongational viscosity χ as a function of time [illegible] LDPE.

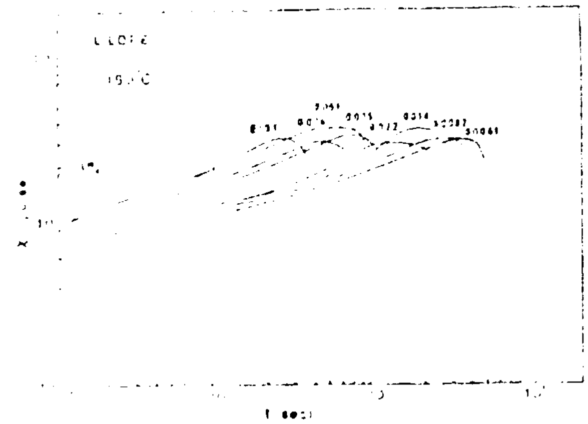

[illegible] elongational viscosity χ as a function of time [illegible]

The apparent elongational viscosities of the HDPE based on maximum values were found by these authors to be much larger than $3\eta_0$ and to decrease with stretch rate.

The response of the LLDPE is of interest. If we remember that this is an ethylene-butene-1 copolymer with small amounts of butene-1, it would seem reasonable to consider the polymer essentially linear. The molecular-weight distributions reported for the LLDPE are similar to those of linear polymers such as commercial polystyrenes, and thermally degraded polypropylenes. We have investigated the elongational flow characteristics of these

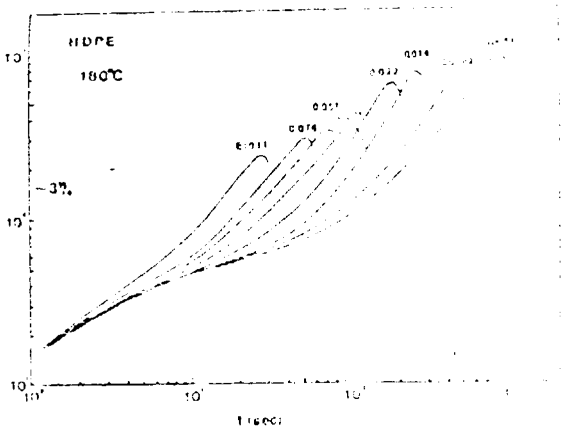

Fig. 4c. Transient elongational viscosity χ as a function [illegible] for HDPE melt

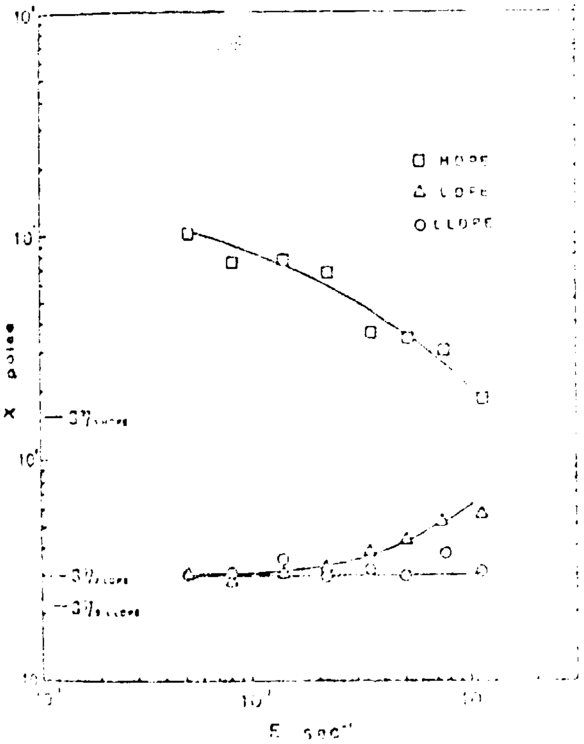

Fig. 5. Steady state elongational viscosities [illegible] for LDPE and LLDPE melts and [illegible] for LDPE and LLDPE melts and [illegible] for HDPE as a function of elongation rate.

three types of polymer melts in previous papers from our laboratories (22–24). Both commercial polystyrene (24) and degraded polypropylenes (22, 23) respond rather similarly to the LLDPE in elongational flow, exhibiting stable elongated filaments and low deformation rate regions where χ is $3\eta_0$.

The view of the above paragraph receives support from the shear viscosity-shear rate and principal normal stress difference-shear stress plots. The HDPE η-γ data is more rapidly decreasing than the LLDPE and the N_1-σ_{12} data is higher. Both of these effects correspond to broader molecular-weight distributions in linear polymer systems (22, 23, 25).

Thus in summary, we seem from isothermal rheological data to be working with two linear polymers, one with a moderately narrow distribution (LLDPE) and one with a rather broad molecular-weight distribution (HDPE). The third material is a long-chain branched polymer (LDPE).

RESULTS OF TUBULAR FILM EXTRUSION EXPERIMENTS

Global Perspective of Kinematics and Stability

We seek to represent the kinematics of the tubular film process in a global manner. There would seem to be three most important kinematic variables for such a representation. These are the drawdown ratio v_L/v_o, the frostline height z_F and the blow-up ratio B. The former two quantities determine the machine direction deformation rates and the latter the transverse direction deformation rates. We set up a three-dimensional space of $v_L/v_o - B - z_F$ in *Fig. 6*. It should be noted, of course, that this is only a first approximation of the kinematics. The detailed bubble shapes for the LDPE, LLDPE, and HDPE actually differ somewhat as shown in *Fig. 7* with the HDPE being more notably thin-necked and inflating in a shorter distance or narrower region of altitude.

The tubular film process operates in a stable condition for only a limited series of operating conditions. Typical unstable bubble shapes are shown in *Fig. 8*. At the various operating conditions one may have stable, unstable, or metastable conditions, the latter representing the existence of two stable states with ready passage between them.

In *Figs. 9–11* we present drawdown ratio (v_L/v_o) – blow-up ratio (B) diagrams for the LDPE, LLDPE, and HDPE melts under study with open circles representing stable behavior, triangles metastable behavior, and closed circles unstable behavior. A frost-line height of 12.0 cm was used.

It is clear from *Figs. 9–11* that the LDPE resin has a much wider operating region of stable behavior than the LLDPE or HDPE do at this frost-line height. At drawdown ratios of 6.0 and greater, the LLDPE seems metastable or unstable under all conditions investigated. At lower v_L/v_o, unstable behavior occurs in the region of B from 1.0 to 2.5. The instability region of the $v_L/v_o - B$ diagram of *Fig. 11* for the HDPE is tunnel-shaped. Unstable behavior occurs between blow-up ratios of 1.0 and 2.2 roughly independent of v_L/v_o. There is, however, no observed tendency towards instability with increased drawdown ratio.

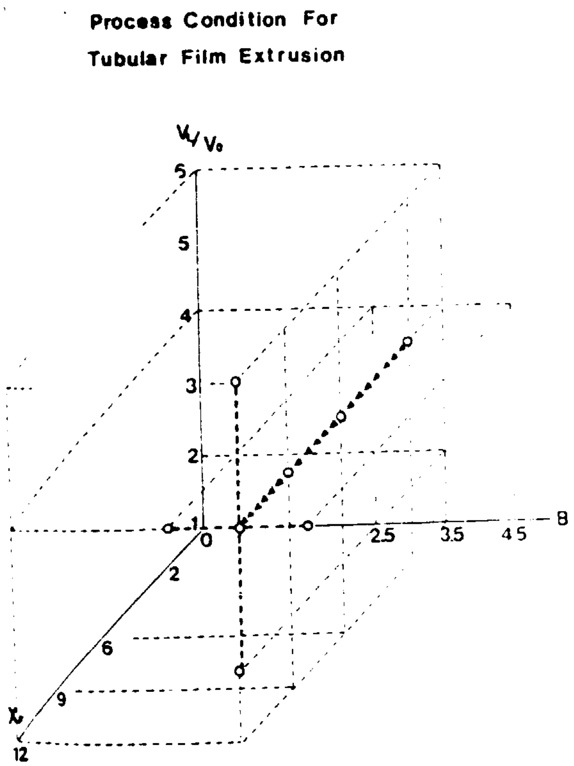
Process Condition For Tubular Film Extrusion

Fig. 6. *Three dimensional space for tubular film kinematics based on drawdown ratio, v_L/v_o, blowup ratio, B, and frost-line height z_F.*

Frost-line height is varied by changing the cooling air flow, with higher air flow decreasing z_F. In *Fig. 12*, we consider the influence of frost line height on the shape of an HDPE tubular film bubble. The higher the frost-line height, the greater the angle made by the film at the position of inflation.

In *Fig. 13a–c*, we present the operating region of stable behavior for the LLDPE at various frost-line heights. It is clear that LLDPE at the lower frostline height has a wider stable region than one at the higher height. The LDPE also has a very wide stable region at the low frost-line height. On the contrary HDPE has almost the same stable region at the different frostline heights and it does not show a wide unstable region under any condition.

Local Kinematics

Stable operating conditions investigated are summarized in *Table 2*. Local velocities v_1 and v_2 as well as elongation rates $\partial v_1/\partial \xi_1$ and $\partial v_2/\partial \xi_2$ have been computed from the motion-picture results. Direct observations of moving material points on the surface of the film were used. Typical results are contained in *Figs. 14, 15*, and *16* for the LDPE, LLDPE, and HDPE, respectively. It may be seen that v_1 increases monotonically, most rapidly in the region of most rapid bubble inflation and plateauing beyond the frost line. The transverse velocity v_2 is zero at small z and then rapidly increases, goes

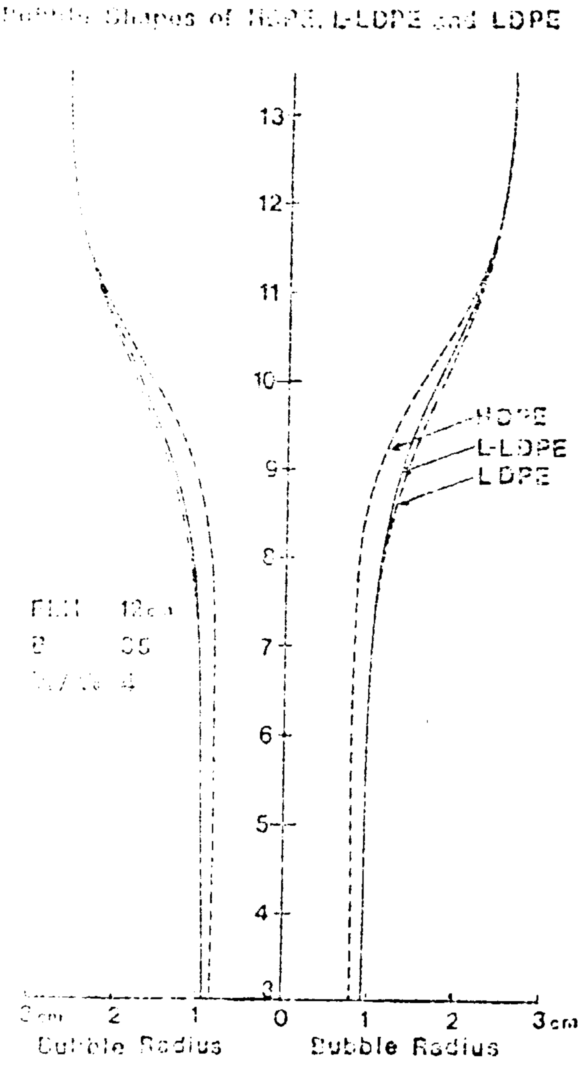

Fig. 7. Bubble shapes for LDPE, LLDPE, and HDPE with v_L/v_0 = 4, B = 3.5 and z_L = 12.0 cm.

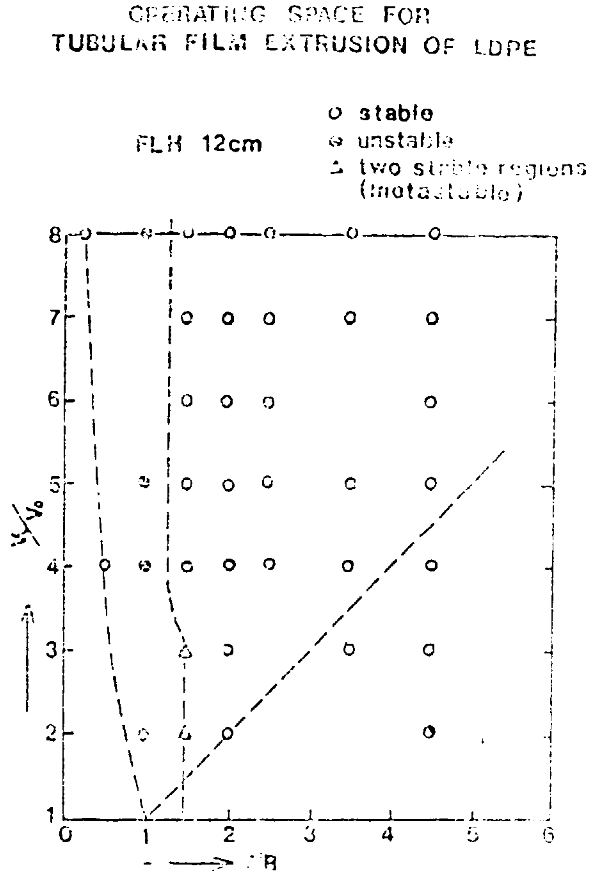

Fig. 9. Drawdown ratio, v_L/v_0 — blowup ratio, B plot for LDPE showing regions of stable, unstable, and metastable behavior, z_L = 12 cm.

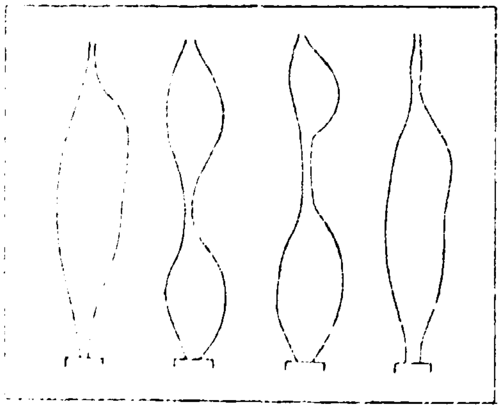

Fig. 8. [illegible] bubbles [illegible]

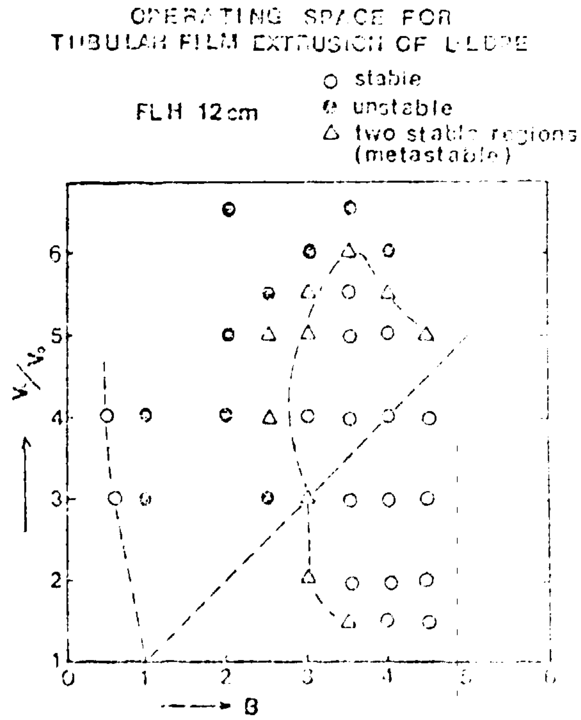

Fig. 10. Drawdown ratio, v_L/v_0 — blowup ratio, B plot for LLDPE showing regions of stable, unstable, and metastable behavior, z_L = 12 cm.

[illegible] a maximum and decreases to zero above the frost line. [illegible] then go through maxima and

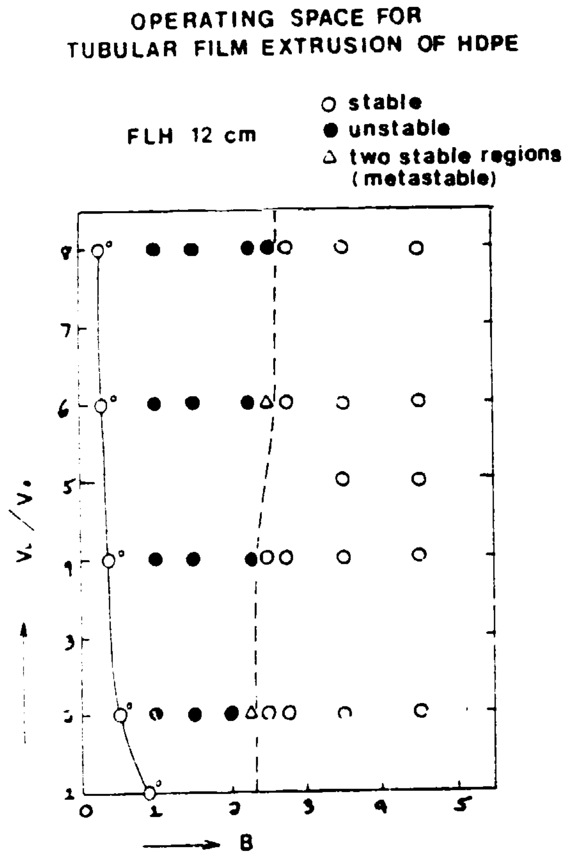

Fig. 11. Drawdown ratio, v_L/v_o, – blowup ratio, B, plot for HDPE showing regions of stable, unstable, and metastable behavior; z_F = 12 cm

decrease to zero above z_F. The behavior is most pronounced with HDPE and least with LDPE.

The influence of frost-line height z_F, at constant v_L/v_o and B on the local deformation rates for the LDPE, LLDPE, and HDPE is shown in *Fig. 17*. In each case increasing frost-line height decreases the maximum value of d_{11}. This is most pronounced for the HDPE and the LLDPE. The maximum d_{22} is independent of z_F at constant v_L/v_o and B for the LDPE and LLDPE but is an increasing function for the HDPE.

The influence of blowup ratio B at constant v_L/v_o and z_F, on the local deformation rates for the LLDPE is shown in *Fig. 18*. Increasing B increases d_{22}.

The effect of drawdown ratio v_L/v_o on the d_{11} and d_{22} profiles along the bubble is shown in *Fig. 19* for the HDPE melts. The magnitudes of d_{11} and d_{22} increase with v_L/v_o.

Dynamics

We now turn to the measured stresses in the bubble for the three polyethylenes. In *Fig. 20*, we plot the take-up tension F_L and machine direction tensile stress, $\sigma_{11}(L)$, as a function of drawdown ratio for the LDPE, LLDPE, and HDPE at a fixed blowup ratio, frost-line height, and extrusion rate. The tensions for the LLDPE and HDPE decrease with v_L/v_o while that for the LDPE increases. If we replot the data in terms of stress σ_{11}, it is found to increase for all the melts, being most rapid in rate of increase for the LDPE.

Fig. 21 shows take up stresses, $\tau_{11}(L)$, of HDPE, LLDPE, and LDPE for different frost-line heights. The higher the frost-line height, z_F, at fixed B, v_L/v_o and extrusion rate, the lower the bubble tension. The take-up stress for LLDPE is the lowest and is most dependent on z_F.

In *Fig. 22*, we plot bubble inflation pressure versus drawdown ratio for the LDPE, LLDPE, and HDPE melts at a fixed blow-up ratio, frost-line height, and extrusion rate. *Figure 23* shows the bubble pressures of HDPE, LLDPE, and LDPE for

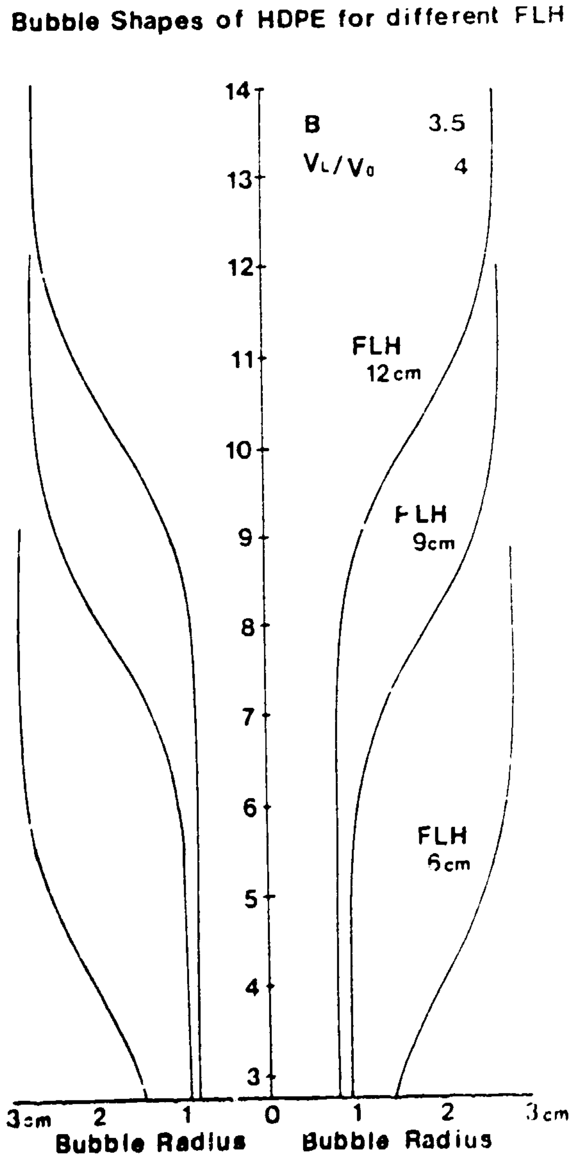

Fig. 12. Influence of frost-line height on bubble shape for HDPE with $v_L/v_o = 4$, $B = 3.5$.

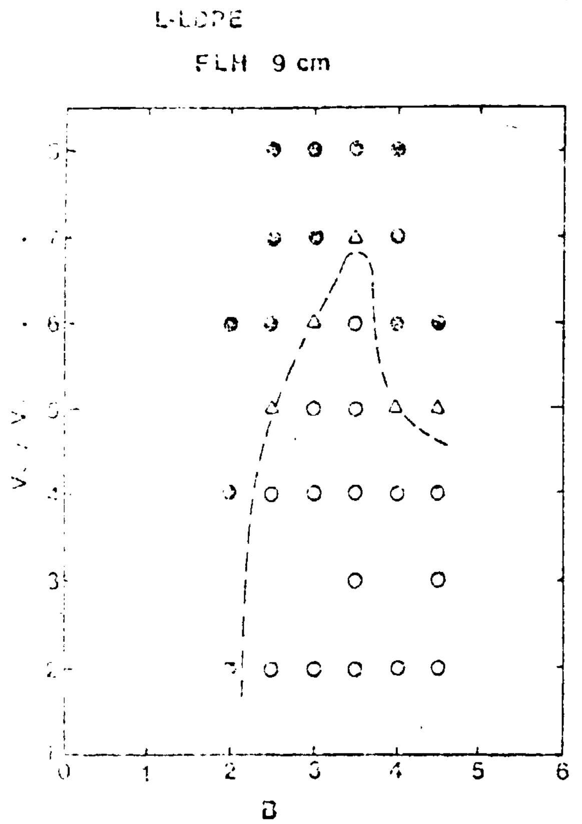

[illegible] Drawdown ratio, v_L/v_0 − blowup ratio, B, plot for LLDPE at different frost-line heights; z_F = 9 cm.

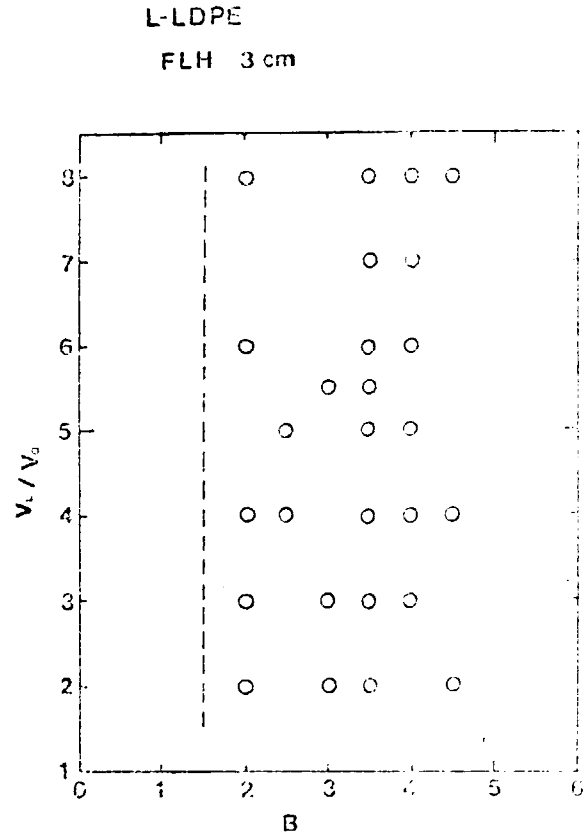

Fig. 13c. Drawdown ratio, v_L/v_0 − blowup ratio, B, plot for LLDPE at different frost-line heights, z_F = 3 cm.

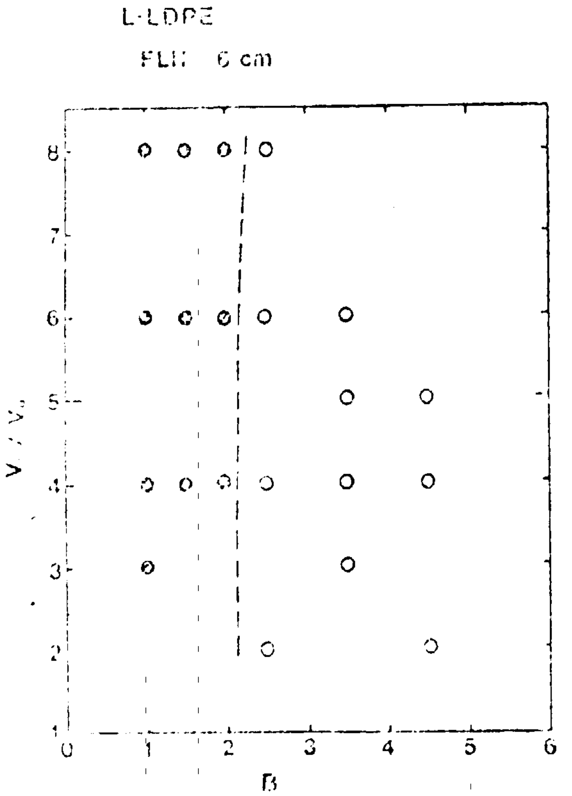

[illegible] Drawdown ratio, v_L/v_0 − blowup ratio, B, plot for LLDPE at different frost-line heights; z_F = 6 cm.

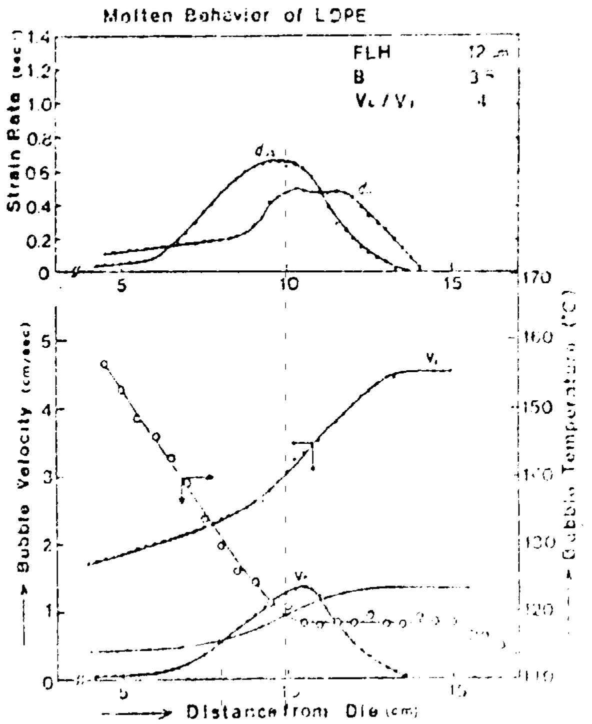

Fig. 14. Local velocities v_1, v_2, deformation rates d_{11}, d_{22} and temperature along the length of the bubble for LDPE with v_L/v_0 = 4, B = 3.5, and z_F = 12 cm.

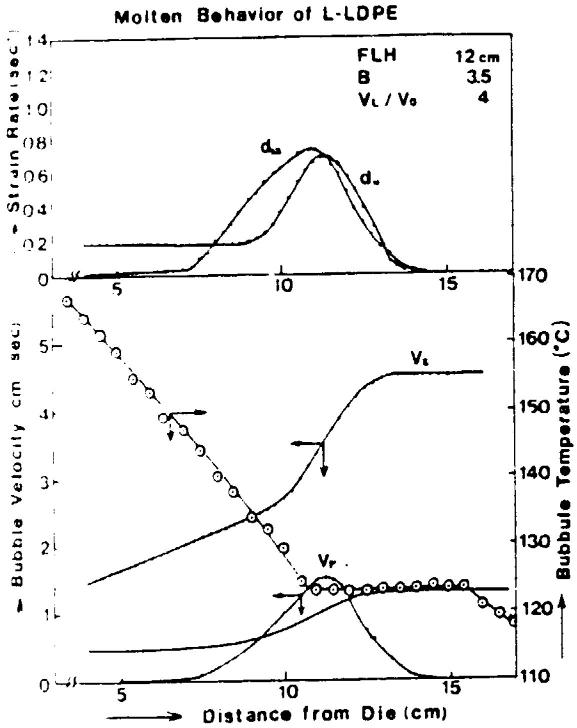

Fig. 15. Local velocities v_1, v_2 deformation rates d_{11}, d_{22}, and temperature along the length of the bubble for LLDPE with $v_L/v_o = 4$, $B = 3.5$, and $z_F = 12$ cm.

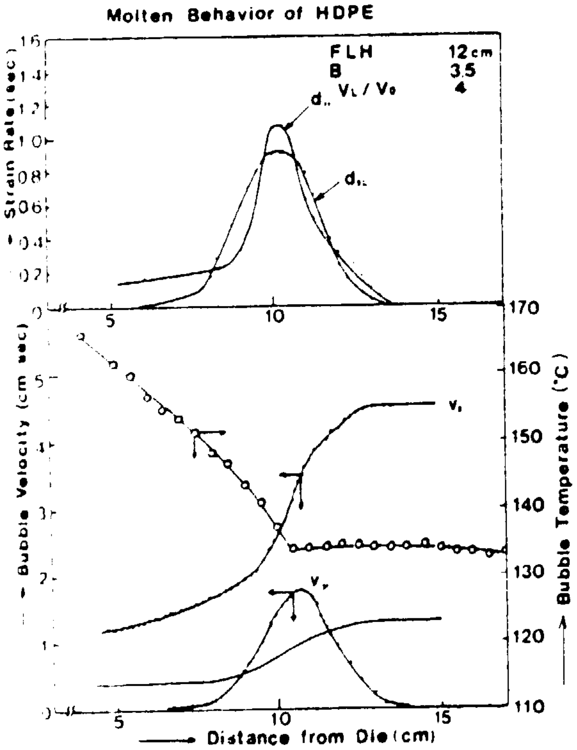

Fig. 16. Local velocities v_1, v_2, deformation rates d_{11}, d_{22}, and temperature along the length of the bubble for HDPE with $v_L/v_o = 4$, $B = 3.5$, $z_F = 12$ cm.

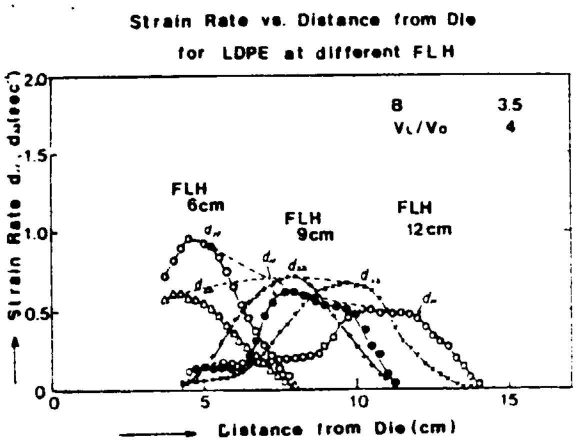

Fig. 17a. Local deformation rates d_{11}, d_{22} along the length of the bubble for various frost-line heights with $v_L/v_o = 4$, $B = 3.5$. LDPE.

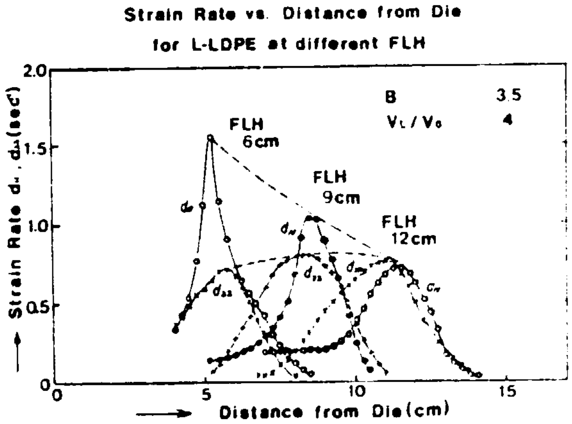

Fig. 17b. Local deformation rates d_{11}, d_{22} along the length of the bubble for various frost-line heights with $v_L/v_o = 4$, $B = 3.5$. LLDPE.

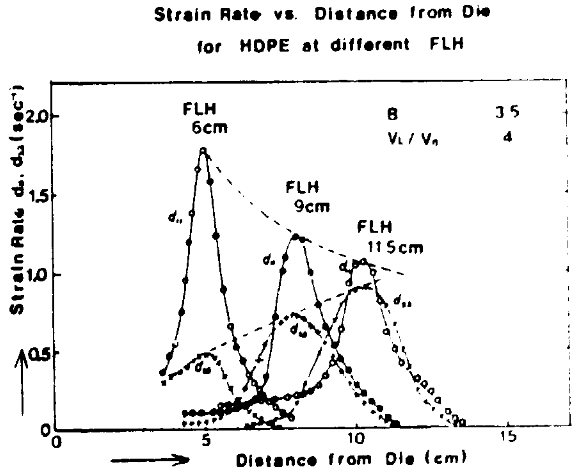

Fig. 17c. Local deformation rates d_{11}, d_{22} along the length of the bubble for various frost-line heights with $v_L/v_o = 4$, $B = 3.5$. HDPE.

different frost-line heights. The LDPE generally requires much higher inflation pressures than the other melts. Inflation pressure increases with in-

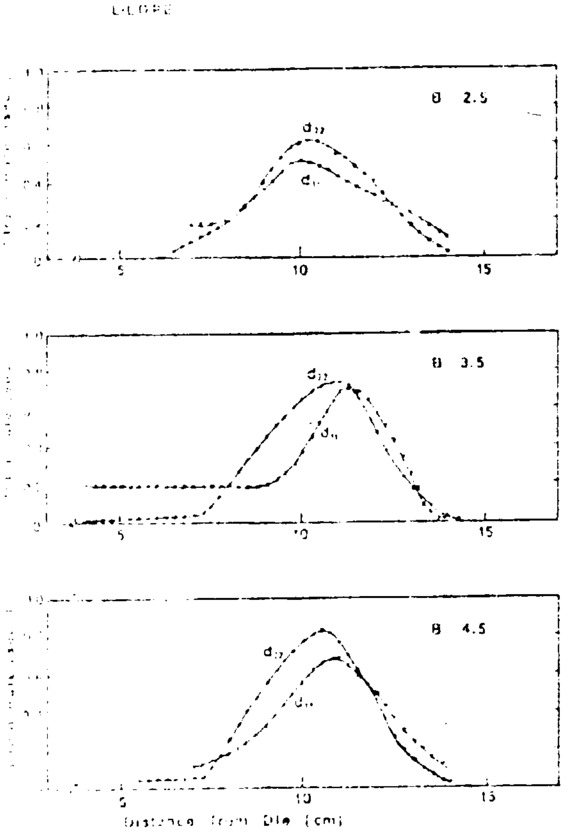

Fig. [illegible]. Local deformation rates d_{11}, d_{33} along the length of the bubble for various blow-up ratios with $v_L/v_0 = 4$; $z_F = 12$ cm

increasing drawdown ratio and decreasing frost-line height.

Figure 24 shows the bubble pressure of HDPE at the various B and v_L/v_0. The higher B, the lower the bubble pressure.

Temperature Profiles

Typical temperature profiles along the machine direction for LDPE, LLDPE, and HDPE films produced with similar kinematics ($v_L/v_0 = 4$, $B = 3.5$, $z_F = 12$ cm) are shown in *Fig. 25*. The temperature decays almost exponentially and reaches a plateau. The values of the temperature at the plateau are 117°C for the LDPE, 122°C for the LLDPE, and [illegible]°C for the HDPE. The plateau is much broader for the HDPE.

As one increases the flow of air out the bubble, the temperature profile shifts to lower distances from the die, resulting in smaller frost-line heights. Cooling air velocity profiles are shown in *Fig. 26*; the resultant temperature profile changes are contained in *Fig. 27* for the LLDPE. The crystallization [illegible] noted.

DISCUSSION

Kinematics and Dynamics

As we have noted earlier, there are differences in the bubble shape when comparisons are made at the same values of v_L/v_0, B, and z_F. The HDPE exhibits a slimmer neck and more rapid increase in bubble diameter. This distinction between the shapes of HDPE and LDPE bubbles may be seen in photographs in papers by Han and Park (5) and Han and Shetty (7).

We may examine our experimental tension data in terms of apparent elongational viscosities. We proceed to do this by fitting our machine direction data to the empirical equation.

$$\sigma_{ij} = -p\delta_{ij} + 2\,\chi_{ef} d_{ij} \tag{11}$$

where χ_{ef} may be dependent upon position. We may write:

$$\sigma_{11} - \sigma_{33} = \sigma_{11} = \chi_{ef}\left(\frac{\partial v_1}{\partial \xi_1} - \frac{\partial v_3}{\partial \xi_3}\right) \tag{12a}$$

$$= \chi_{ef}\left(\frac{Q\cos\theta}{2\pi RH}\left(-\frac{1}{R}\frac{dR}{dz} - \frac{2}{H}\frac{dH}{dz}\right)\right) \tag{12b}$$

In *Fig. 28*, we plot the second invariant of the deformation rate II_d, defined as

$$\mathrm{II}_d = tr\,\underline{d}^2 = d_{11}^2 + d_{22}^2 + d_{33}^2 \tag{13}$$

and the elongational viscosity, χ_{ef}, versus distance from the die. These lower lines show the apparent elongational viscosity χ_{ef} and the upper lines show the second invariant of elongational rate II_d

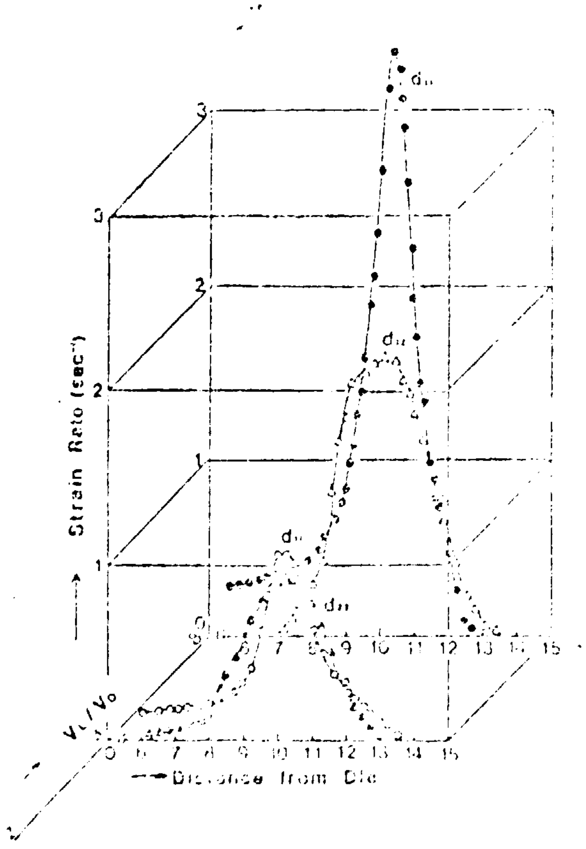

Fig. [illegible]. Local deformation rates d_{11}, d_{33} of HDPE along the length of the bubble for various drawdown ratios (z_F = 12 cm, B = 3.5 [illegible])

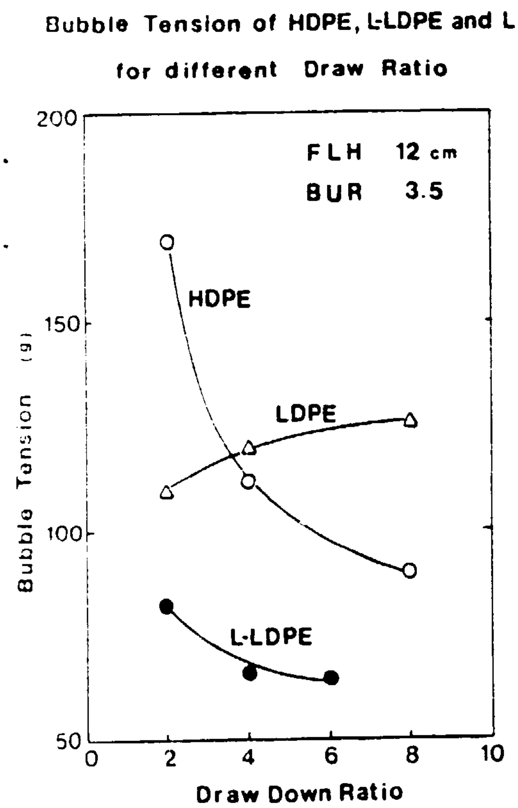

Fig. 20a. Bubble F_L tension and take-up stress σ_{11} (L) as a function of draw down ratio v_L/v_o with $B = 3.5$, $z_f = 12$ cm Tension, F.

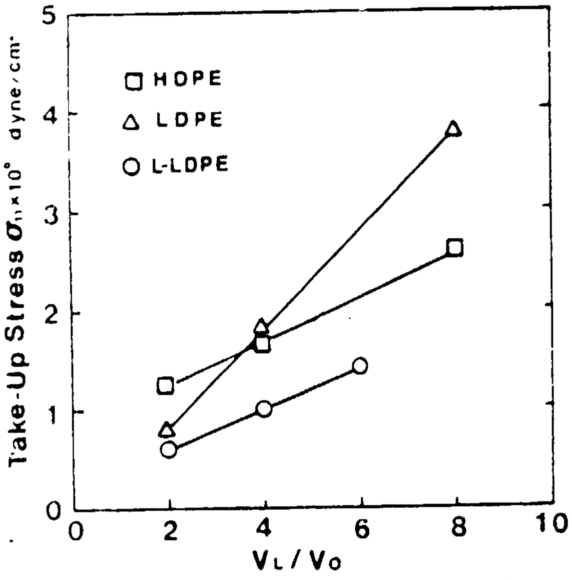

Fig. 20b. Bubble F_L tension and take-up stress σ_{11} (L) as a function of draw down ratio v_L/v_o with $B = 3.5$, $z_f = 12$ cm Stress, σ_{11}.

For HDPE the apparent elongational viscosity decreases very slowly between 5 and 7.5 cm from the die. However, as bubble diameter and elongational rate increases, χ_{ef} decreases rapidly and shows a sharp peak. After crystallization begins, the apparent elongational viscosity increases rapidly and approaches infinity. The elongational rate curve also shows a very sharp peak.

For the LDPE, the apparent elongational viscosity decreases slowly and does not exhibit a sharp peak. After crystallization begins, the apparent elongational viscosity increases slowly. The elongational rate also changes slowly. The apparent

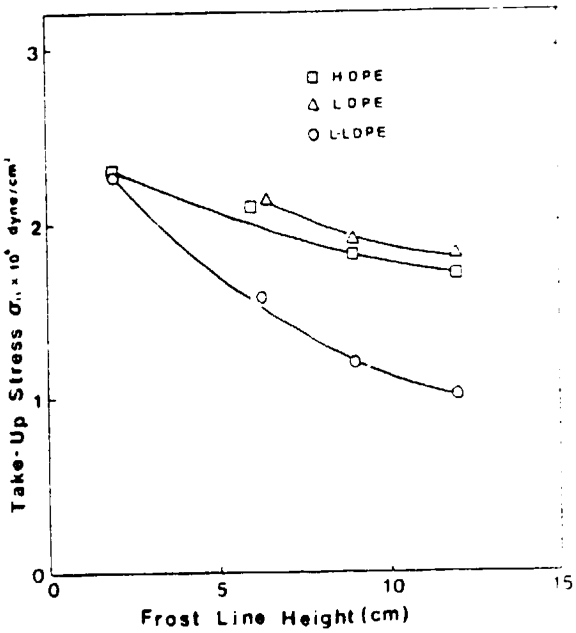

Fig. 21. Bubble take-up stress as a function of frost-line height (B = 3.5, $v_L/v_o = 4$).

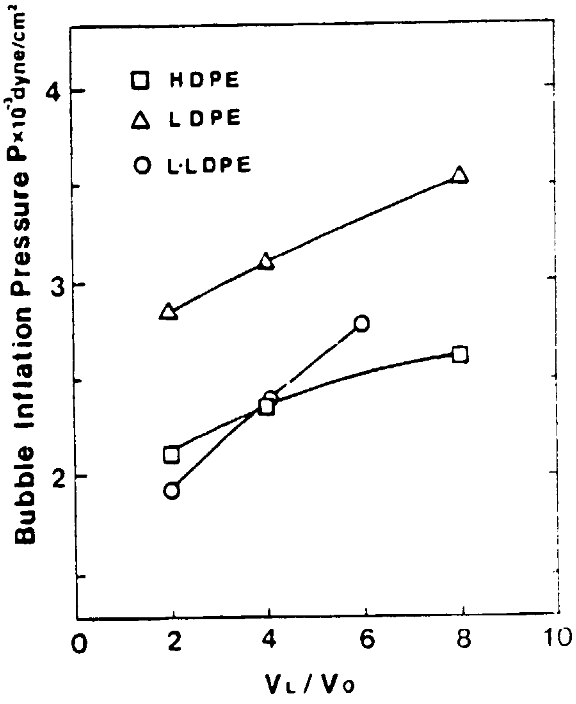

Fig. 22. Bubble inflation pressure as a function of draw down ratio v_L/v_o ($B = 3.5$, $z_f = 12$ cm)

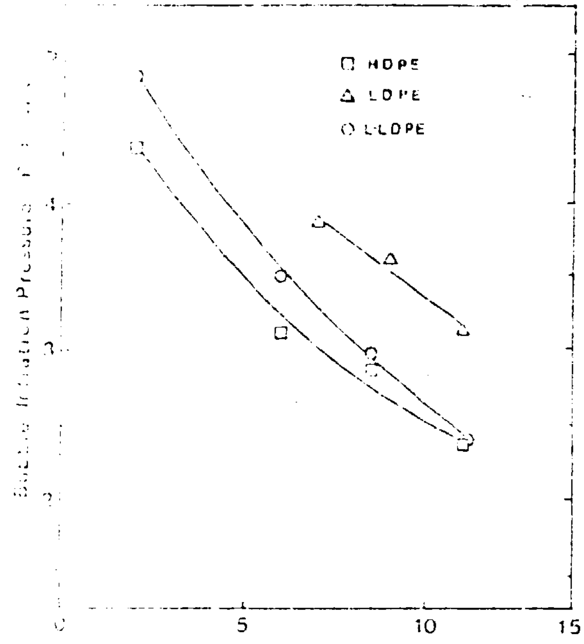

[illegible] Bubble inflation pressure as a function of frost-line [illegible] L_f = 12 cm

elongational viscosity of the LLDPE and its elongational rate show a tendency intermediate between HDPE and LDPE.

The apparent elongational viscosities seem more influenced by elongational rate than bubble temperature before crystallization begins. As the elongational rate increases, the apparent elongational viscosity decreases. After crystallization begins the elongational rate decreases and the apparent elongational viscosity increases rapidly.

Figure 29 shows the apparent elongational viscosity and the elongational rate vs. the distance from the die for different frostline heights in the case of HDPE. This figure shows both the apparent elongational viscosities and the elongational rate profiles exhibit very similar patterns. In the case of a frost line height of 6 cm, χ_f increases more rapidly than the other two cases.

Bubble Stability

The problem of bubble stability was first described in a paper by Han and Park (6) and was later expanded upon by Han and Shetty (7). They present detailed descriptions of the instability contrasted to the so-called "draw resonance" phenomenon observed in film casting from slit dies (27, 28). Some examinations of the influence of drawdown on blow-up ratio are contained in their work.

A theoretical stability analysis of instabilities due [illegible] Newtonian [illegible] has been given by Yeow (29). It is not possible to make detailed comparison of this theory with our experimental results because we are concerned with non-isothermal behavior of viscoelastic polymer melts. Yeow's results are presented in terms of [illegible] and [illegible] variables, specifically for each input disturbance frequency, the instability occurs at a corresponding value of

$$T = \frac{R_0 L_f}{\eta Q}, \qquad A = \frac{\pi R_0^3 \Delta p}{\eta Q}, \qquad X_F = \frac{z}{R} \qquad (11a)$$

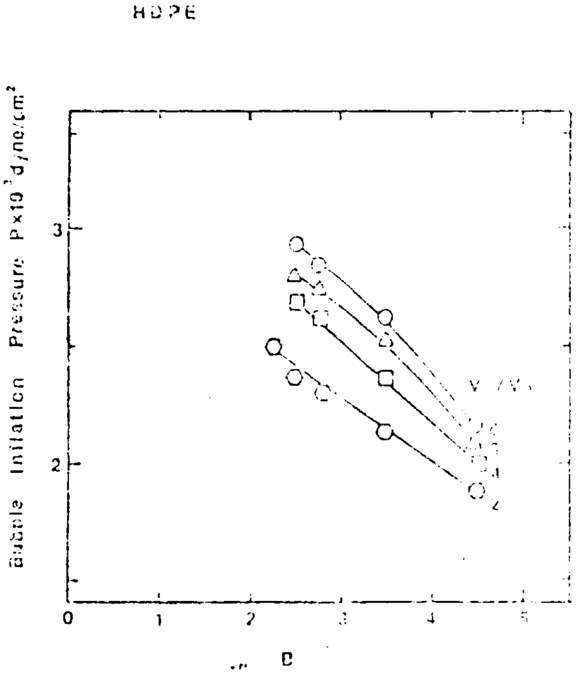

Fig. 24. Bubble inflation pressure of HDPE as a function of blow-up ratio B

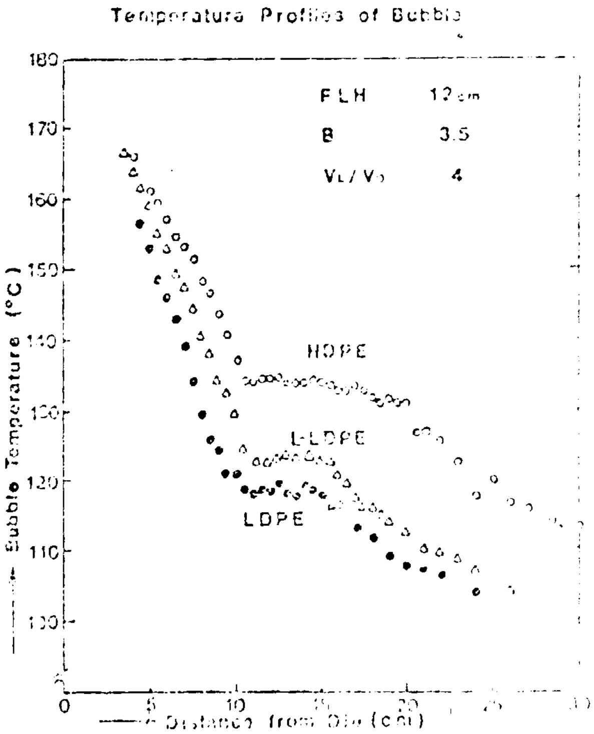

Fig. 25. Temperature profile along the bubble for HDPE, LDPE and LLDPE [illegible]

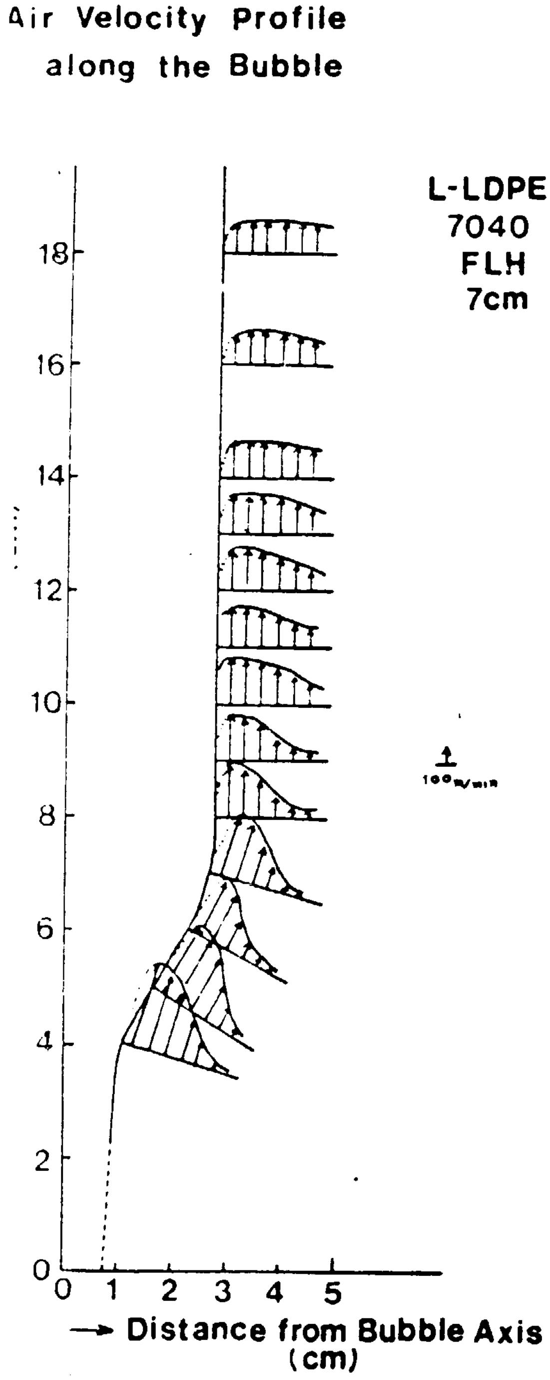

Fig. 26. Air velocity profiles along the bubble.

$$H^{\circ} = \frac{H_L}{H_o} \qquad B = \frac{R_L}{R_o} \qquad X_F = \frac{z_F}{R_o} \qquad (14b)$$

re R_o is the annular die radius. Yeow presents al stability curves on plots of T vs A or H^* vs pecific X_F. We present plots of the latter type 30a and 30b. In *Fig. 30a* we compare the ity of LDPE, LLDPE, and HDPE at $X_F = 12/$ 16 while in *Fig. 30b* we contrast the LLDPE results for X_F equal to 4, 8, 12, and 16. In comparison to Yeow's calculations we find our bubbles tend to be unstable.

It would seem reasonable to discuss the differing bubble stabilities of LDPE, LLDPE, and HDPE in

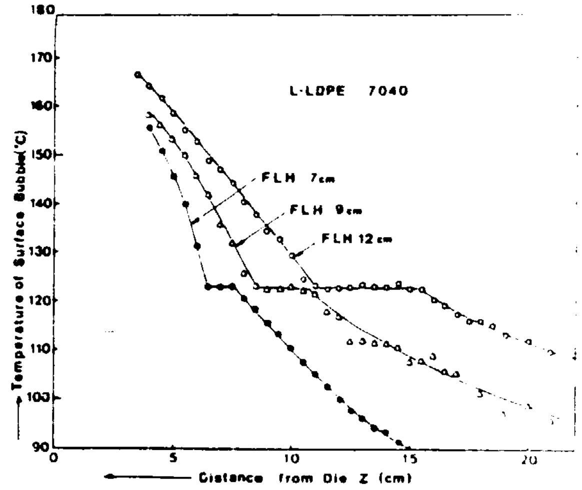

Fig. 27. Bubble temperature profile as a function of frost-line height.

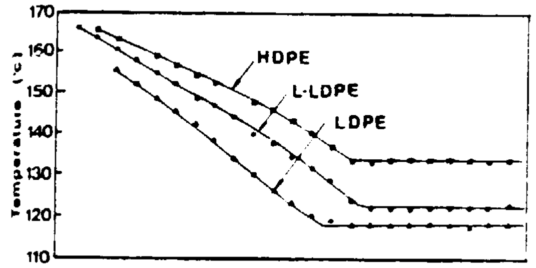

Fig. 28a. Temperature profiles for LDPE, LLDPE, and HDPE along the length of the bubble.

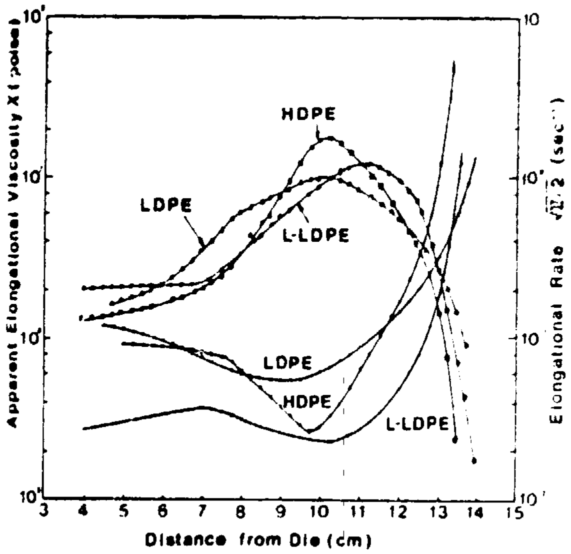

Fig. 28b. Apparent elongation viscosities and elongation rates along the length of the bubble.

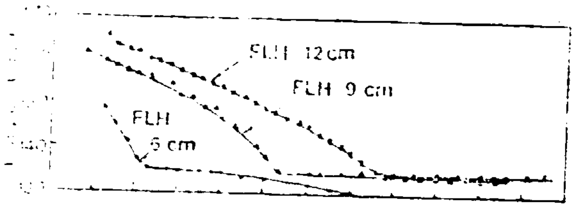

[illegible] along the length of the bubble for [illegible] frost-line height.

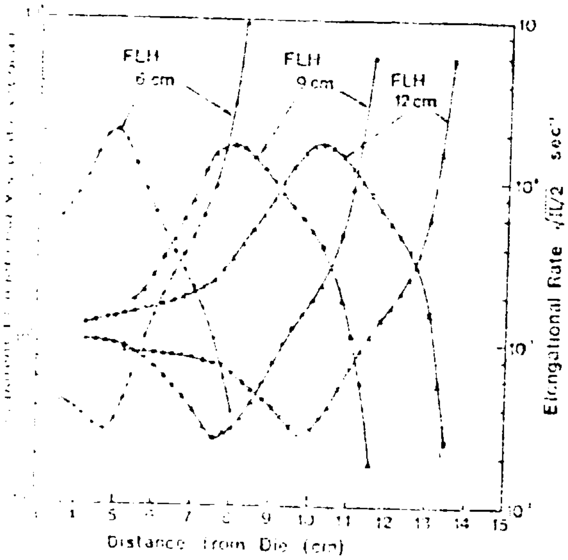

[illegible] and Π_d versus distance [illegible]

terms of elongational flow behavior. This does mark the relative sensitivity of melts to disturbances. Elongation-rate hardening should be stabilizing. Figure 5 thus suggests that stability should occur along the lines LDPE > LLDPE > HDPE. Compare the discussions of draw resonance by White and Ide (30). Figure 30a implies the LDPE is most stable and LLDPE unstable. As frost-line height is decreased, HDPE becomes more unstable than LLDPE.

Heat Transfer

Heat transfer coefficients can be computed from temperature profiles in the regions where crystallization does not occur. This is carried out directly using Eq 10.

In Fig. 31 we plot the heat-transfer coefficient as a function of distance from the die for the LDPE, LLDPE, and HDPE melts. The data is similar and may be expressed [illegible] $c_a = 4$, $B = 3.5$).

$$z < 8 \text{ cm} \qquad h = c_1 \ (\text{Kcal/m}^2\text{hr}^\circ\text{C}) \qquad (15a)$$

$$z > 8 \text{ cm} \qquad h = \frac{c_2}{z^a} \ (\text{Kcal/m}^2\text{hr}^\circ\text{C}) \qquad (15b)$$

where c_1 is [illegible] for LDPE, 40 for LLDPE and 35 for HDPE. c_2 has values of 1140 for z_f of 7 cm, 1020 for z_f of 9 cm, and 830 for z_f of 12 cm; a is about [illegible]

Figure 32 shows the influence of z_f on h for the LLDPE near the die. Values of h up to 70 are found for z_f equal to 7 cm. The variation of frost line height is accomplished through changes in air velocity, blowing along the length of the bubble. Increasing air velocity decreases frost line height. Measurements of air velocities and their influence on frost-line height are indicated in Fig. 30. This suggests a modified correlation of form:

$$z < K \text{ cm} \qquad h = C'U \qquad (16a)$$

$$z > K \text{ cm} \qquad h = \frac{C_2}{z^a} \qquad (16b)$$

where U_i is the initial air velocity.

It would be desirable to express h in a dimensionless form of the type describing originally by Nusselt (31, 32), i.e. as

$$\frac{hL}{k_{air}} = C\left[\frac{LU\rho_{air}}{\eta_{air}}\right]^{a}\left[\frac{c\eta_{air}}{k_{air}}\right]^{b} \qquad (17a)$$

or

$$\frac{hL}{k_{air}} = C'\left(\frac{LU\rho_{air}}{\eta_{air}}\right)^{a} \qquad (17b)$$

where k is thermal conductivity, c, heat capacity, and the subscript "air" refers to values for air. Equation 17b is a simpler form which may be used. Since air is the only medium involved, the second

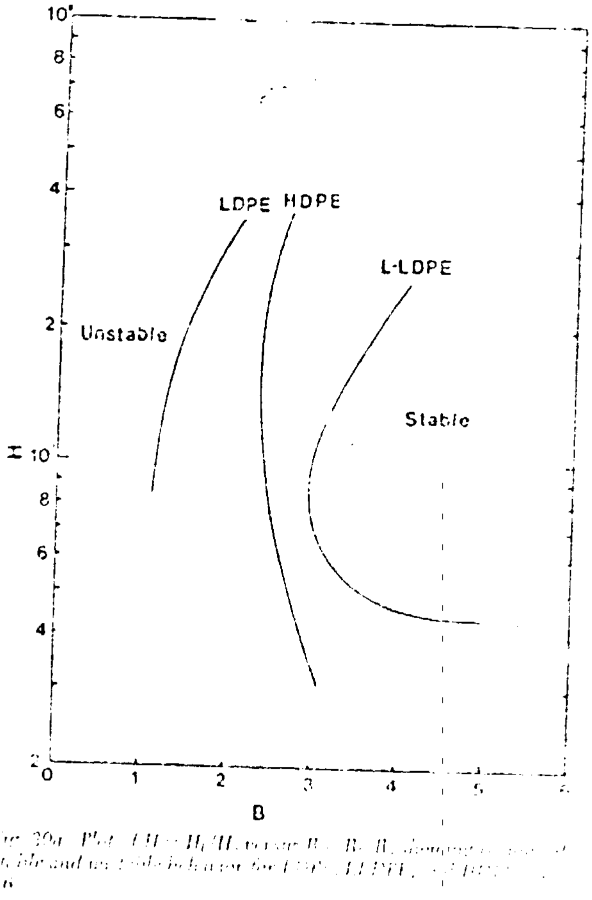

Fig. 30a. Plot [illegible] versus B [illegible] stable and unstable behavior for LDPE, LLDPE, [illegible]

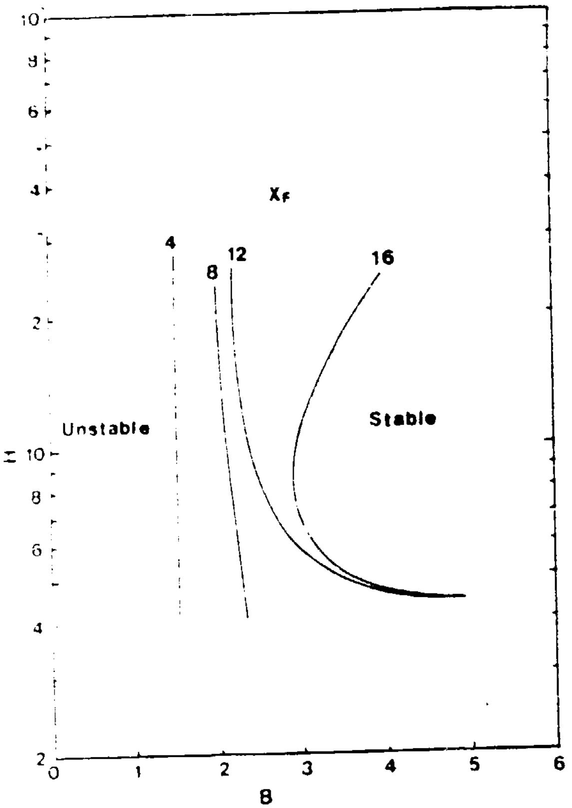

Fig. 30b. Plot of $H = H_f/H_o$ versus $B = R_f/R_o$ showing regions of stable and unstable behavior for LLDPE, $X_F = 4, 8, 12, 16$.

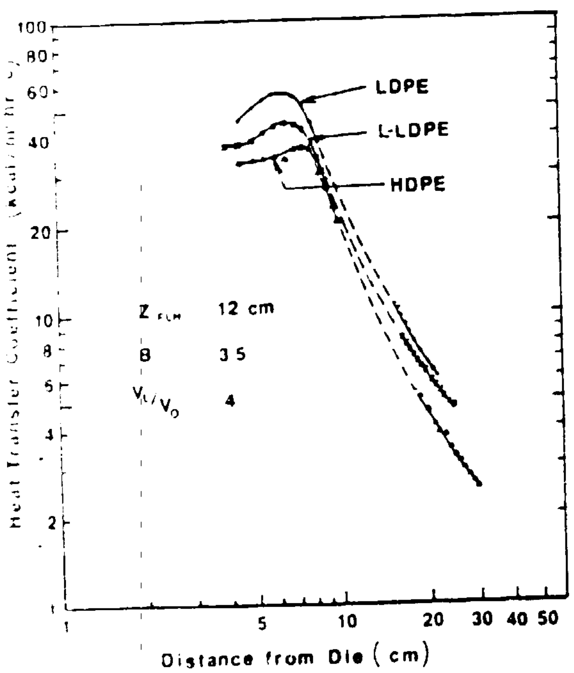

Fig. 31. Plot of heat-transfer coefficient versus position for LDPE, L-LDPE, and HDPE bubbles.

dimensionless group, the Prandtl number can be combined into C to give C'.

Before we consider applying *Eq 18*, we should decide the initial point to measure L from on the bubble. We chose the position of the maximum of the local heat-transfer coefficient to define as $L = 0$. Those initial points are 6.5 cm for a frostline height of c_F of 7 cm, 6.5 cm for z_F of 9 cm, and 7.0 cm for z_F of 12 cm from the die exit. L is the vertical distance from the initial point. The maximum air velocities are chosen to be the value of U.

Figure 33 shows the relation between the Nusselt number and the Reynolds number, $LU\rho/\eta_{air}$. Our results are correlated by

$$\frac{hL}{k_{air}} = 0.043 \left(\frac{LU\rho_{air}}{\eta_{air}}\right)^{0.76} \qquad (18)$$

The lowest the frost line height, the better the correlation of *Eq 18* is found.

Above the frostline our data is best correlated by

$$h = 2.5\ V_{max}^{1.6} \qquad (19)$$

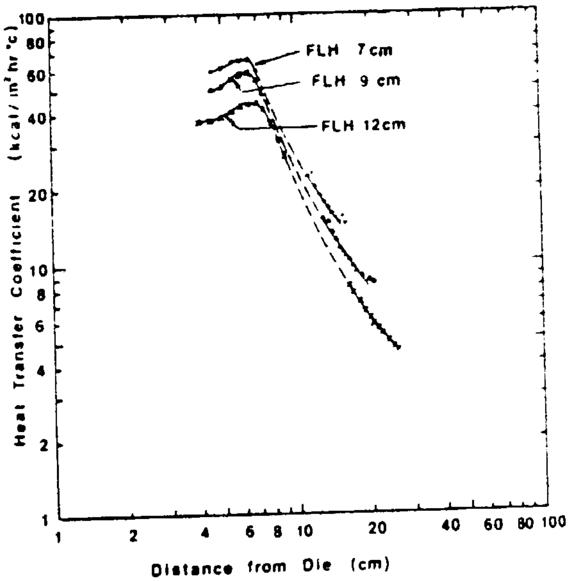

Fig. 32. Plot of heat transfer coefficient h versus position on bubble for LLDPE an $z_F = 7, 9$ and 12 cm $v_f/v_o = 4$, $B = 3.5$

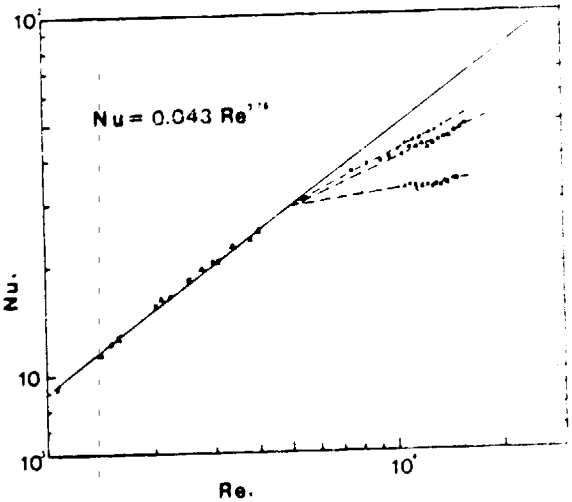

Fig. 33. Nusselt number as a function of air Reynold number

shown in *Fig. 34*. V_{max} is the local maximum air velocity.

This is similar to the predictions of Menges and Predöhl (1). We summarize our representations of the heat transfer in *Fig. 35*.

Crystallization Rate

In the temperature profiles for each of the three polymer melts, a plateau corresponding to crystallization occurs. The variation of crystallinity with position in this region may be estimated from *Eq 16* and the heat transfer coefficients computed in the previous section. The heat of crystallization ΔH_f is taken as 49 cal/g and the specific heat by 0.56 cal/g °C.

In *Fig. 36*, we plot crystallinity versus time for the three polyethylenes. For the same v_L/v_0 (4), blowup ratio (3.5) and frost-line height (12 cm), the rates of crystallization seem similar.

Table 3 shows the crystallization rate and air velocity at the frost-line height. In the case of HDPE, there is a small temperature difference between the die exit and crystallization temperature, so the air velocity is lower than for the LDPE and LLDPE. From this point of view, the crystallization rate of HDPE is the fastest during the tubular film process as the cooling rate is lower.

The final level of crystallinity is computed to be 0.31 for the LDPE, 0.28 for the LLDPE, and 0.41 for the HDPE. This compares to values of 0.48, 0.45, and 0.72 obtained from densities of the films one week later. This suggests about 60 percent of the crystallization occurs in the plateau region.

The influence of air velocity U_a through frost line height, z_L, on crystallization rate is shown in *Fig. 37*. Increasing U_a and decreasing z_L increases crystallization rates.

Table 4 shows the relation between the air velocity at the frost line height and the half life [illegible]. The result shows the crystallization rate strongly depends on the cooling rate.

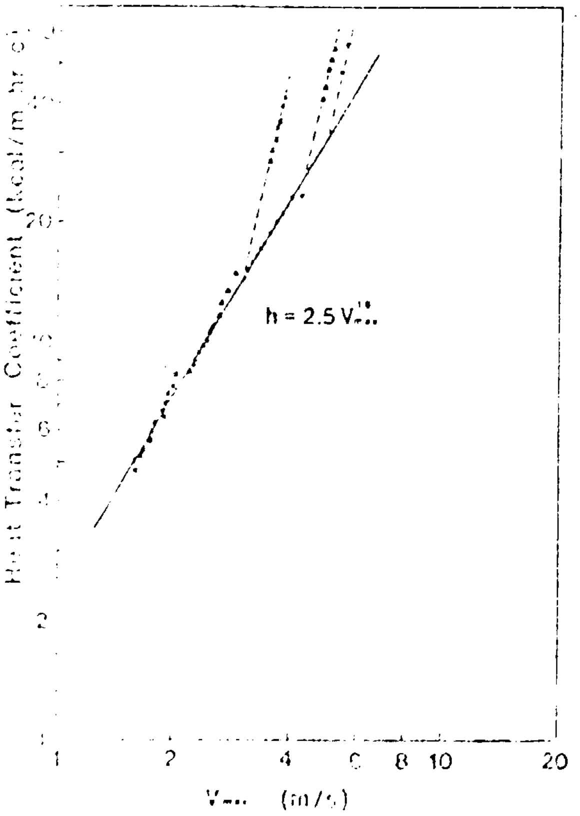

Fig. 34. Heat [illegible] as a function of maximum air [illegible]

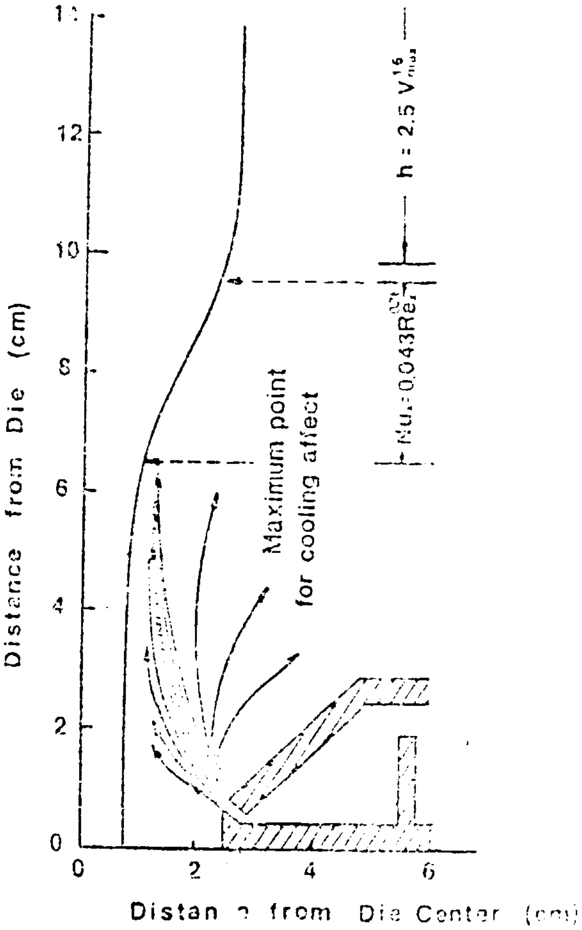

Fig. 35. Regimes of heat transfer observed in tubular film extrusion.

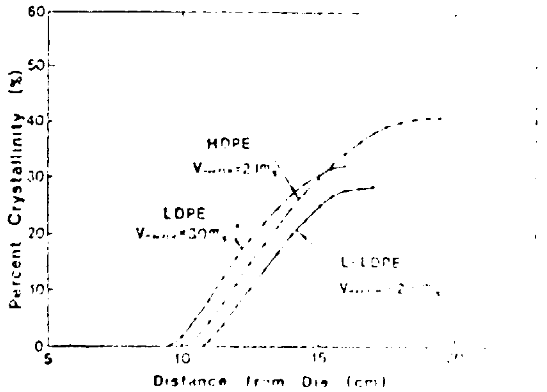

Fig. 36. Crystallinity as a function of position along the line for LDPE, LLDPE, and HDPE. [illegible]

Table 3. Development of Crystallinity in Tubular Film Extrusion

	HDPE	L-LDPE	LDPE
$t_{1/2}$ (sec)	8.0	6.0	6.3
$V_{Max,FLH}$ (m/s)	2.1	2.8	3.0
Plateau temperature (°C)	134.5	122.0	117.0
Plateau level of crystallinity (−)	0.41	0.28	0.31
Final crystallinity obtained from density	0.72	0.45	0.48

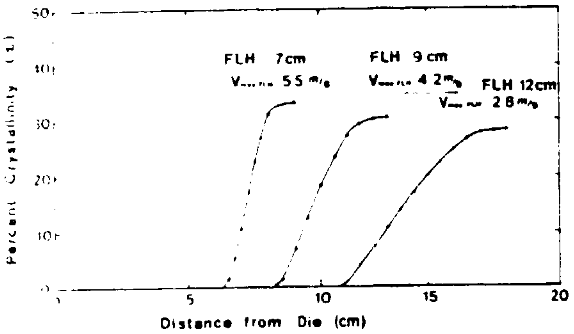

Fig. 37. Crystallinity as a function of position along the bubble for HDPE with $v_L/v_0 = 4$, $B = 3.5$ at various frost-line heights.

Table 4. Crystallization as a Function of Frost-line Height For HDPE

Frost-line Height (Z)	Air Velocity $V_{Max,FLH}$ (M/S)	Crystallization Temp (°C)	Cooling Stress (Dynes/cm²)	Half Time t/½ (sec)
7	5.5	122	1.52×10^6	2/3
9	4.2	122	1.20×10^6	3.6
12	2.8	122	1.0×10^6	6.3

ACKNOWLEDGMENT

We acknowledge the support of one of us (T. Kanai) during the course of this research by Idemitsu Petrochemical. We would like to thank Union Carbide and Phillips Petroleum for supplying the polymer used in this study.

REFERENCES

1. G. Menges and W. Predohl, *Plastverarbeiter*, 23, 338 (1972/3).
2. W. Ast, Kunststoffe, 63, 427 (1973).
3. W. Ast, *Kunststoffe*, 64, 146 (1974).
4. R. Farber and J. M. Dealy, *Polym. Eng. Sci.*, 14, 435 (1974).
5. C. D. Han and J. Y. Park, *J. Appl. Polym. Sci.*, 19, 3257 (1975).
6. H. H. Winter, *Pure Appl. Chem.*, 55, 943 (1983).
7. C. D. Han and J. Y. Park, *J. Appl. Polym. Sci.*, 19, 3291 (1975). C. D. Han and R. Shetty, *IEC Fundam.* 16, 49 (1977).
8. W. F. Maddams and J. E. Preedy, *J. Appl. Polym. Sci.*, 22, 2721, 2739 (1978).
9. K. J. Choi, J. L. White, and J. E. Spruiell, *J. Appl. Polym. Sci.*, 25, 2777 (1980).
10. K. J. Choi, J. E. Spruiell, and J. L. White, *J. Polym. Sci. Polym. Phys. Ed.*, 20, 27 (1982).
11. Y. Shimomura, J. E. Spruiell, and J. L. White, *Polym. Eng. Rev.*, 2, 417 (1983); also, *J. Appl. Polym. Sci.*, 27, 2663 (1982).
12. J. R. A. Pearson, "Mechanical Principles of Polymer Processing," Pergamon, Oxford (1966).
13. J. R. A. Pearson and C. J. S. Petrie, *J. Fluid Mech.*, 40, 1 (1970).
14. J. R. A. Pearson and C. J. S. Petrie, *J. Fluid Mech.*, 42, 609 (1970).
15. J. R. A. Pearson and C. J. S. Petrie, *Plast. Polym.*, 38, 85 (1970).
16. T. Alfrey, *SPE Trans.*, 5, 68 (1965).
17. C. J. S. Petrie, *Plast. Polym.* 44, 259 (1974).
18. C. D. Han and J. Y. Park, *J. Appl. Polym. Sci.*, 19, 3277 (1975).
19. M. H. Wagner, *Rheol. Acta*, 15, 40 (1976).
20. K. Walters, "Rheometry," Chapman and Hall, London (1975).
21. J. L. White in "Rheometry: Industrial Applications," edited by K. Walters, Wiley, N. Y. (1980).
22. W. Minoshima, J. L. White, and J. E. Spruiell, *Polym. Eng. Sci.*, 20, 1166 (1980).
23. H. Yamane and J. L. White, *Polym. Eng. Rev.*, 2, 167 (1983).
24. Y. Ide and J. L. White, *J. Appl. Polym. Sci.*, 22, 1061 (1978).
25. K. Oda, J. L. White, and E. S. Clark, *Polym. Eng. Sci.*, 18, 25 (1978).
26. W. Minoshima, Ph.D. Dissertation in Polymer Engineering, University of Tennessee, Knoxville (1983).
27. A. Bergonzoni and A. J. DiCresci, *Polym. Eng. Sci.*, 6, 45 (1966).
28. S. Kase, *J. Appl. Polym. Sci.*, 18, 3279 (1974).
29. Y. L. Yeow, *J. Fluid Mech.*, 75, 577 (1976).
30. J. L. White and Y. Ide, *J. Appl. Polym. Sci.*, 22, 3057 (1978).
31. E. R. G. Eckert and R. M. Drake, "Heat and Mass Transfer," 2nd ed, McGraw-Hill, N. Y. (1959).
32. R. B. Bird, W. E. Stewart, and E. N. Lightfoot "Transport Phenomena," Wiley, N. Y. (1960).

Appendix B

Orientation and Morphology of High-Density Polyethylene Film Produced by the Tubular Blowing Method and its Relationship to Process Conditions

KYUNG-JU CHOI, JOSEPH E. SPRUIELL, and JAMES L. WHITE,
Polymer Engineering, The University of Tennessee, Knoxville, Tennessee 37916

Synopsis

The orientation and crystallinity of a series of high-density polyethylene (HDPE) tubular films is characterized using wide-angle x-ray scattering pole-figure analysis and birefringence. The films ranged from uniaxial to equal biaxial. The data were used to compute biaxial orientation factors which were then plotted on an orientation-factor triangle diagram. It was shown, within the range of conditions studied, that both the crystalline biaxial orientation factors were unique functions of the stresses exerted on the bubble at the freeze line. Both correlations are the same as those developed by Dees and Spruiell for melt-spun HDPE fibers. SAXS measurements on the films suggest lamellar structures in both uniaxial and biaxial films.

INTRODUCTION

Polyethylene film is probably the largest-volume polymeric product, and its structural characterization is thus of considerable interest. Not only is the structure of the film of concern, but also the relationship of structure to the details of its formation. Most polyethylene film is produced by the tubular process. Several authors have published experimental investigations of the tubular-film extrusion of polyethylene or of the films produced by this process.[1-13] Some of these investigators[1-3,6,10-13] have studied the crystalline character of the films, including in many cases careful quantitative evaluations of the crystalline orientation. However, they generally do not know the applied stress fields in the process and often nothing of the kinematics. The recent papers of Maddams and Preedy[10-13] are the most important studies of the development of crystalline orientation and morphology of polyethylene film to date.

The present authors and their co-workers have carried out extensive investigations of orientation and crystalline morphology development, particularly with polystyrene[14-18] and polyolefins.[19-22] The studies with polystyrene indicate that the orientation developed in the melt during flow is frozen in at vitrification. The rheo-optical law relating birefringence and stress may be applied at vitrification to yield the level of birefringence in the product. Oda, White, and Clark[14] originally hypothesized and verified this for shear flow, uniaxial elongational flow, and melt spinning of polystyrene. More recently we[18] verified this for the tubular film extrusion of the same polymer. In-plane and out-of-plane birefringences were related to draw tension and bubble pressure. Dees and Spruiell[19] have found that orientation development in melt spinning of polyethylene under a range of conditions may be correlated with the spinning

Journal of Polymer Science: Polymer Physics Edition, Vol. 20, 27–47 (1982)

CCC 0098-1273/82/010027-21$02.10

stress. This has been found to be true for polypropylene as well by Spruiell and White[21] and by Nadella et al.[22] These results suggest that the crystalline orientation developed in tubular-film extrusion of polyolefins should also be determined by the applied stress fields.

The purpose of the present paper is to present an experimental study of the development of structure in tubular extrusion of high-density polyethylene film under known conditions of applied stress. We seek in this study to determine if the orientation is determined by the stress and the extent to which its levels differ from the predictions of the rheo-optical law. This paper then represents an extension of both our earlier studies of melt spinning of polyolefins[19–22] to tubular-film extrusion as well as an extension of our tubular-film investigations of polystyrene[18] to polyolefins. To a limited extent our perception of structure development in tubular-film extrusion is similar to the pioneering study of Rohn[23] on polybutene-1. However, he did not make orientation and stress measurements on tubular film, but inferred the nature of their relation from orientation measurements made on fibers and stress measurements made on molded slabs elongated at elevated temperature.

BACKGROUND

Orientation Representation

Orientation in polymer systems may be represented at varying levels of sophistication. At the simplest level, orientation factors representing the second moment of the orientation distribution may be defined. Methods such as birefringence, x-ray diffraction, and dichroism may be used to measure such second moments for the amorphous and crystalline regions of a polymer. In crystalline polymers, wide-angle x-ray scattering (WAXS) and construction of pole figures[2,3,10,11,24–26] allow a complete representation of the distribution of reflecting plane normals in space. In many instances the distribution of polymer chains and crystallographic axes can also be determined.

It is necessary for us to discuss orientation-factor representation of second moments of the distribution. Such representations date to the work of Hermans and his co-workers,[27–29] who used the anisotropic characteristics of the polarizability tensor for the case of uniaxial fiber orientation. The representation of biaxial orientation in terms of orientation factors was initiated by Stein[30] and has since been considered by Kawai, Nomura, Kimura, and Kagiyama[31–34] in a series of papers, as well as by Desper and Stein[25] and by White and Spruiell.[35] The work of Stein and Kawai et al. defines orientation factors in terms of Euler's angles expressed with respect to a characteristic (e.g., machine) direction. This is an awkward formulation and results in asymmetry of representation with respect to the machine and transverse directions. Wilchinsky[24] and Desper and Stein[25] suggested using values of averaged mean-square cosines of angles between crystallographic axes and machine and transverse directions. White and Spruiell[35] proposed biaxial orientation factors based upon the anisotropy of the polarizability or attenuation tensors and the angles used by Wilchinsky, Desper, and Stein. The Hermans orientation factor for the polymer chain axis is replaced in this system by the two orientation factors

$$f_1^B = 2\,\overline{\cos^2\phi_{c1}} + \overline{\cos^2\phi_{c2}} - 1 \tag{1a}$$

$$f_2^B = 2\,\overline{\cos^2\phi_{c2}} + \overline{\cos^2\phi_{c1}} - 1 \tag{1b}$$

where the subscript c refers to the chain direction, while subscripts 1 and 2 refer to the reference directions (e.g., machine and transverse directions). For the case of uniaxial orientation about the machine direction we have

$$\overline{\cos^2\phi_{c2}} = \overline{\cos^2\phi_{c3}} \tag{2}$$

which leads to

$$f_{1c}^{B} = \tfrac{1}{2}(\overline{3\cos^2\phi_{c1}} - 1) \tag{3a}$$

$$f_{2c}^{B} = 0 \tag{3b}$$

For uniaxial orientation one of the biaxial orientation factors reduces to the Hermans orientation factor, while the other is equal to zero. These orientation factors have been applied by Matsumoto, Fellers, and White[36] and by the present authors[18] to express orientation in polystyrene film.

We may express these orientation factors in terms of an orientation triangle as shown in Figure 1.[35] This triangle is a region in f_1^B vs. f_2^B space set about the origin (0,0) with corners at (1,0), (0,1), and (−1, −1). The axes represent uniaxial orientation with respect to either reference axis; the position (1,0) represents complete orientation in the machine direction, (0,1) complete orientation in the transverse direction, and (−1, −1) orientation perpendicular to the plane of these two directions (i.e., parallel to the sheet normal).

In the case of crystalline polymer, White and Spruiell suggest that eq. (1) may be generalized to all three crystallographic axes:

$$f_{1j}^{B} = 2\,\overline{\cos^2\phi_{j1}} + \overline{\cos^2\phi_{j2}} - 1 \tag{4a}$$

$$f_{2j}^{B} = 2\,\overline{\cos^2\phi_{j2}} + \overline{\cos^2\phi_{j1}} - 1 \tag{4b}$$

where j represents the a, b, and c crystallographic axes. For orthorhombic crystals six orientation factors are interrelated by two orthogonality relationships,

$$\overline{\cos^2\phi_{a1}} + \overline{\cos^2\phi_{b1}} + \overline{\cos^2\phi_{c1}} = 1 \tag{5a}$$

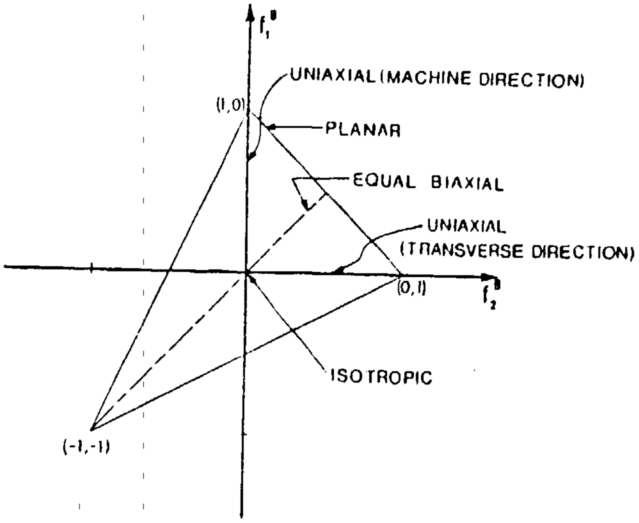

Fig. 1. Orientation triangle for White–Spruiell orientation factors.

$$\overline{\cos^2\phi_{a2}} + \overline{\cos^2\phi_{b2}} + \overline{\cos^2\phi_{c2}} = 1 \tag{5b}$$

Consequently,

$$f^B_{1a} + f^B_{1b} + f^B_{1c} = 0 \tag{6a}$$

$$f^B_{2a} + f^B_{2b} + f^B_{2c} = 0 \tag{6b}$$

Only four of the six orientation factors are independent.

Orientation-Stress Relationship

It is well known in flowing melts of flexible polymer chains that birefringence is related to stress through the rheo-optical law[38–42]:

$$\mathbf{n} = (\tfrac{1}{3}\,\mathrm{tr}\mathbf{n})\mathbf{I} + C\mathbf{P}$$

or

$$n_i - n_j = C(P_i - P_j) = C(\sigma_i - \sigma_j) \tag{7}$$

Here **P** is the deviatoric stress tensor, σ the total stress tensor, and the single index indicates a principal value. If this birefringence is due to chain orientation rather than form birefringence or "bond bending," as it appears to be in melts and vitrified glasses, the birefringence may be related to the orientation factors of eq. (1) through[35]

$$(n_1 - n_3)/\Delta^0 = f^B_1, \quad (n_2 - n_3)/\Delta^0 = f^B_2 \tag{8}$$

where Δ^0 is the maximum or intrinsic birefringence.

We may combine eqs. (8) and (7) together to yield

$$f^B_1 = (C/\Delta^0)(\sigma_1 - \sigma_3) \tag{9a}$$

$$f^B_2 = (C/\Delta^0)(\sigma_2 - \sigma_3) \tag{9b}$$

or

$$f^B_1 - f^B_2 = (C/\Delta^0)(\sigma_1 - \sigma_2) \tag{9c}$$

The rheo-optical law implies a linear relation between orientation and the stress in the melt.

If a glass is a "frozen" melt without change in structural order, one would expect chain orientation to be preserved in vitrification. The orientation in glasses should then be related linearly to the stresses acting at vitrification. This has been reported for uniaxial extension and shear flow of polystyrene[14]; the melt spinning of polyethylene terephthalate,[43] polystyrene,[14] and high-impact polystyrene[44]; biaxial stretching of polystyrene[45]; and tubular-film extrusion of polystyrene.[18]

It does not follow that orientation in crystalline polymers should be predictable from the rheo-optical law because of the orientation changes that accompany crystallization.

Kinematics and Dynamics

The kinematics and dynamics of tubular-film extrusion, while receiving the attention of Alfrey,[46] first obtained detailed consideration in the papers of Pearson and Petrie.[47–49] If we take 1 as the machine direction, 2 as the circumferential direction, and 3 as the thickness direction we may write the velocity gradients in a tubular-film process (see Fig. 2) as follows:

$$\frac{\partial v_1}{\partial \xi_1} = \frac{Q\cos\theta}{2\pi Rh}\left(-\frac{1}{h}\frac{dh}{dz} - \frac{1}{R}\frac{dR}{dz}\right) \tag{10a}$$

$$\frac{\partial v_2}{\partial \xi_2} = \frac{Q\cos\theta}{2\pi Rh}\frac{1}{R}\frac{dR}{dz} \tag{10b}$$

$$\frac{\partial v_3}{\partial \xi_3} = \frac{Q\cos\theta}{2\pi Rh}\frac{1}{h}\frac{dh}{dz} \tag{10c}$$

where Q is the extrusion rate, R the bubble radius at any elevation z, and θ the angle between the axis of the bubble z and a tangent to the surface of the bubble. The derivation of eq. (10a) involves an assumption of constant density which is not fully satisfied because of cooling and eventual crystallization of the melt. Bearing this approximation in mind we proceed to consider different special kinematic cases. For uniaxial extension

$$\frac{\partial v_2}{\partial \xi_2} = \frac{\partial v_3}{\partial \xi_3}, \quad \frac{1}{R}\frac{dR}{dz} = \frac{1}{h}\frac{dh}{dz} \tag{11a}$$

while for planar extension

$$\frac{\partial v_2}{\partial \xi_2} = 0, \quad \frac{1}{R}\frac{dR}{dz} = 0 \tag{11b}$$

For equal biaxial extension

$$\frac{\partial v_1}{\partial \xi_1} = \frac{\partial v_2}{\partial \xi_2}, \quad -\frac{1}{R}\frac{dR}{dz} - \frac{1}{h}\frac{dh}{dz} = \frac{1}{R}\frac{dR}{dz} \tag{11c}$$

Generally it is only possible to maintain such kinematics at a point in the film

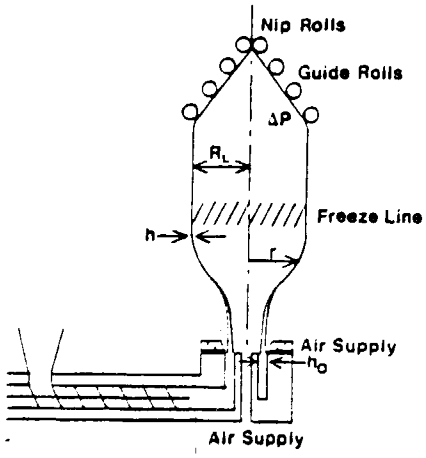

Fig. 2. Tubular film process.

and not for a range of positions along the machine direction. The ability of a polymer melt to maintain these kinematics depends upon its rheological properties. If, however, we presume that a melt could maintain uniaxial kinematics then eq. (11a) can be integrated to give

$$V_L/V_0 = 1/B^2 \tag{12a}$$

where B is the blowup ratio R_L/R_0 (subscript L designates the takeup, 0 the extension die). For planar extension, we have from eq. (11b)

$$B = 1 \tag{12b}$$

For equal biaxial extension, eq. (11c) leads to

$$V_L/V_0 = B \tag{12c}$$

If the drawdown and blowup ratios of eq. (12) are used, one will obtain detailed kinematics which are on the average uniaxial, planar extensional, and equal biaxial. Experimental studies of the kinematics of tubular-film extrusion can be found in the papers of Farber and Dealy,[50] Han and Park,[8] and Choi et al.[18]

The force balance on tubular films is most rapidly developed from shell theory[51] as has been described by Alfrey.[46] The first explicit derivation and discussion was in a series of papers by Pearson and Petrie.[47–49] These authors show that it simplifies to the expressions

$$F_L = 2\pi R h \sigma_{11} \cos\theta + \pi \Delta p (R_L^2 - R^2) \tag{13a}$$

$$\Delta p = h\sigma_{11}/R_1 + h\sigma_{22}/R_2 \tag{13b}$$

where σ_{11} is the stress in the machine direction and σ_{22} that in the circumferential (transverse) direction; F_L is the drawdown force; Δp is the bubble pressure; and R_1 and R_2 are the principal radii of curvature of the film. At the freeze line, we have

$$R_1 = \infty, \quad R_2 = R_L, \quad \cos\theta = 1, \quad \sigma_{11} = F_L/2\pi R_L h_L, \quad \sigma_{22} = R_L \Delta p/h_L \tag{14}$$

Experimental studies of tubular-film extrusion dynamics are reported by Han and Park,[8] Wagner,[52] and the present authors.[18]

EXPERIMENTAL

Materials

The polymer used in this study was a Chemplex 6009 high-density polyethylene with a melt index of 0.98.

Film Preparation

The tubular film was produced with a ¾-in. Rainville extruder with an annular blown film die (inside diameter of 1.496 cm and outside diameter 1.605 cm). The extrusion temperature was 200°C.

A series of three films (labeled 1, 2, 3) were prepared under uniaxial conditions with drawdown ratios V_L/V_0 of 5.2–16.4. A second series of films (labeled 4, 5, 6) was prepared at a blowup ratio of 2.2 with drawdown ratios of 3.4–10.6. Two

TABLE I
Kinematics of Tubular-Film Formation

Sample	Drawdown (V_L/V_0)	Film thickness (μ)	Blowup ratio B
1	5.2	228	0.31
2	10.0	148	0.23
3	16.4	74.0	0.22
4	3.4	44.5	2.2
5	6.5	25.4	2.2
6	10.6	13.3	2.3
7	5.04	15.1	4.7
8	7.94	5.1	9.8

films (labeled 7 and 8) were prepared with blowup ratios of 4.7 and 9.8 with approximately equal drawdowns.

The conditions for film preparation are described in Tables I and II. Pressures inside of the bubble were measured with a manometer. Tensions in the film were determined with a Tensitron web tension sensor.

Density

The level of crystallinity was determined at 23°C using a water–isopropyl alcohol gradient density column with a range 0.9200–0.9700 g/cm^3. The crystalline fraction X was determined through the expression

$$X = (\rho_c/\rho)(\rho - \rho_a)/(\rho_c - \rho_a) \tag{15}$$

where ρ_c is the crystalline density and ρ_a is the amorphous density.

Birefringence

Birefringence measurements were made representing the difference in index of refraction between the machine and transverse directions, $\Delta n_{12} = n_1 - n_2$, and between the machine and thickness directions, $\Delta n_{13} = n_1 - n_3$. These

TABLE II
Pressures, Tensions, and Stress Fields Applied in the Tubular-Film Process

Sample	Drawdown tension F (N)	Blowup pressure Δp (Pa)	Machine direction stress σ_{11} at and above freeze line (MPa)	Transverse direction stress σ_{22} at and above freeze line (MPa)
1	1.5	0	0.42 ± 0.01	0
2	1.3	0	0.62 ± 0.01	0
3	1.0	0	1.1 ± 0.01	0
4	1.5	160	0.34 ± 0.01	0.066
5	1.4	160	0.51 ± 0.01	0.11
6	1.2	160	0.80 ± 0.09	0.22
7	1.1	63	0.32 ± 0.09	0.15
8	1.2	45	0.48 ± 0.20	0.68

measurements were carried out using an instrument equivalent to that of Stein.[53] This instrument is equipped with a Babinet compensator and provides a means for both rotating and tilting the sample in the polarized light beam.

Wide-Angle X-Ray Scattering (WAXS)

Pole figures were prepared by the WAXS technique of Heffelfinger and Burton[54] using Cu K_α radiation.

Sheets of polyethylene blown film were carefully stacked, clamped, and glued so as to maintain their machine and transverse directions parallel. Smaller, cube-shaped samples (about 1.5 mm edge length) were cut from the original "sandwiches." The latter samples were mounted on a glass rod and placed in a General Electric XRD-5 x-ray diffractometer equipped with a single-crystal orienter. With the diffractometer set a a fixed angle 2θ for diffraction from a chosen set of diffraction planes, the sample can be tilted and rotated by the single-crystal orienter in order to determine the intensity function $I(\phi,\alpha)$ needed for pole-figure plotting or measurement of the $\overline{\cos^2\phi}$ functions needed for computation of orientation factors. Here ϕ is the angle between the normals to the (hkl) diffracting planes (poles) and a reference direction such as the machine direction, while α measures the rotation of the poles about the chosen reference direction; i.e., ϕ and α are the radial and circumferential angles of the pole with respect to Cartesian reference axes chosen along the machine direction (MD), transverse direction (TD), and normal direction (ND) of the film.

A point count procedure was used to collect data at 5° increments in ϕ and α over one hemisphere (2π steradians). This procedure was facilitated by computer control of the diffractometer and single-crystal orienter.

Experiments carried out on random compression-molded samples showed that no absorption corrections were necessary for measurements made using the above-described sample geometry. Correction for background and peak overlap was carried out by a combination of the methods of Nichols[55] and Aggarwal and Tilley[56] using 2θ scans obtained at several different α and ϕ values.

The corrected intensity data were normalized to pole density values in "time random" units by dividing each intensity value by the intensity a random sample would have exhibited under the same experimental conditions. This latter value was determined from the total integrated intensity over the surface of the pole figure.

In order to evaluate the six orientation functions represented by eqs. (2a) and (2b), it is necessary to measure four *cosine square averages*, e.g., $\overline{\cos^2\varphi_{a_1}}$, $\overline{\cos^2\phi_{a_2}}$, $\overline{\cos^2\phi_{b_1}}$, and $\overline{\cos^2\phi_{b_2}}$. Both $\overline{\cos^2\phi_{a_1}}$ and $\overline{\cos^2\phi_{a_2}}$ are obtained from the 200 pole-figure intensity data through

$$\overline{\cos^2\phi_{a_1}} = \frac{\int_0^\pi \int_0^{2\pi} I_{200}(\phi_1,\alpha_2)\cos^2\phi_1 \sin\phi_1 \, d\alpha_1 \, d\phi_1}{\int_0^\pi \int_0^{2\pi} I_{200}(\phi_1,\alpha_1)\sin\phi_1 \, d\alpha_1 \, d\phi_1} \tag{16a}$$

and

$$\overline{\cos^2\phi_{a_2}} = \frac{\int_0^\pi \int_0^{2\pi} I_{200}(\phi_1,\alpha_2)\cos^2\phi_2 \sin\phi_1 \, d\alpha_2 \, d\phi_2}{\int_0^\pi \int_0^{2\pi} I_{200}(\phi_2,\alpha_2)\sin\phi_2 \, d\alpha_2 \, d\phi_1} \tag{16b}$$

TABLE III
Birefringence and Densities of Tubular Film

Sample	Birefringence × 10^3			Density
	Δn_{12}	Δn_{13}	Δn_{23}	ρ (g/cm^3)
1	1.51	1.93	0.42	0.957
2	9.85	10.5	0.66	0.95[illegible]
3	18.1	19.2	1.10	0.956
4	3.97	5.21	1.24	0.955
5	8.78	11.0	2.22	0.954
6	11.9	16.5	4.62	0.953
7	5.81	9.66	3.85	0.955
8	1.87	10.0	8.15	0.953

where ϕ_1 measures the angle between the 200 pole and the machine direction and ϕ_2 measures the angle between the 200 pole and the transverse direction. The integrations are carried out numerically by the computer that controls the diffractometer. In the same manner, $\overline{\cos^2\phi_{b_1}}$ and $\overline{\cos^2\phi_{b_2}}$ are determined from the 020 intensity distribution. It is also possible to determine the four independent average cosine-squared values from the 110 and 200 pole-figure (intensity) data using Wilchinsky's treatment.[57] Because the intensity of the 110 reflection is stronger than that of the 020 reflection, this procedure is often preferable. In

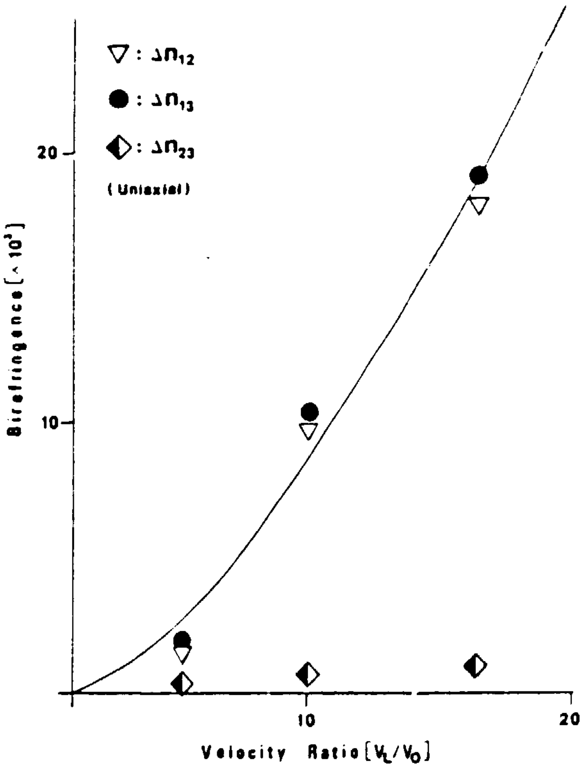

Fig. 3. Birefringences Δn_{12}, Δn_{13}, and Δn_{23} as a function of drawdown ratio for uniaxial films.

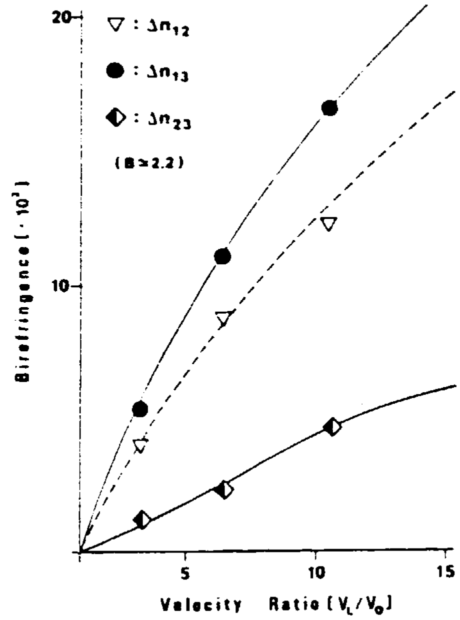

Fig. 4. Birefringences Δn_{12}, Δn_{13}, and Δn_{23} as a function of drawdown ratio for films with constant blowup ratio.

the present study, both methods were used on some samples in order to provide a check on the results.

Small-Angle X-Ray Scattering (SAXS)

SAXS patterns were obtained using a modified Kiessig camera with pinhole collimation. The camera was mounted on a Rigaku–General Electric rotating-anode x-ray generator. Air scattering was reduced by evacuating the camera. The sample to film distance was 40 cm and exposure times of two to ten hours were used.

RESULTS

The birefringences and densities measured on the polyethylene films are listed in Table III. The birefringences Δn_{12}, Δn_{13}, and Δn_{23} are plotted as a function of drawdown ratio V_L/V_0 in Figures 3 and 4 for the uniaxial and constant-blowup-ratio series samples.

For the series of films which are approximately uniaxial

$$\Delta n_{13} \approx \Delta n_{12} > 0, \quad \Delta n_{23} \approx 0 \tag{17a}$$

with the magnitude of Δn_{13} increasing with drawdown.

For the constant-blowup-ratio series of samples

$$\Delta n_{13} > \Delta n_{12} > \Delta n_{23} > 0 \tag{17b}$$

In the case of the approximately biaxial film

$$\Delta n_{13} \approx \Delta n_{23} > \Delta n_{12} \tag{17c}$$

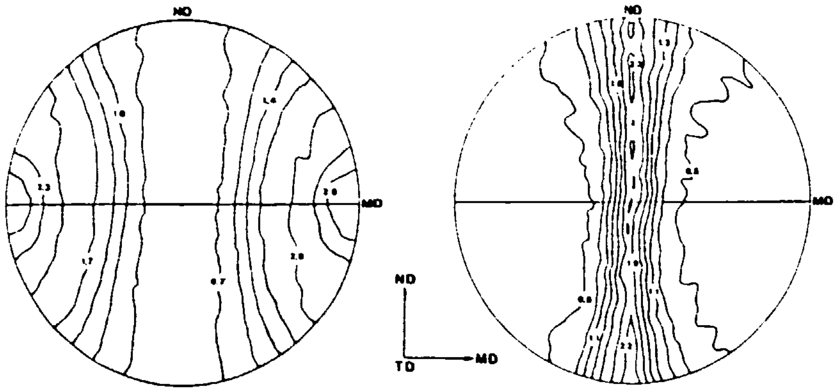

#1 - (200)   #1 - (020)

Fig. 5. Pole figures for (200) and (020) planes for film 1.

Examples of the 200 and 020 pole distributions are shown in Figures 5–8 for samples 1, 3, 6, and 8 of Table I. Samples 1 and 3 are approximately uniaxial cases corresponding to the lowest (sample 1) and the highest (sample 3) drawdown). Sample 6 corresponds to the highest-drawdown sample with a blowup ratio of 2.2, while sample 8 is the nearly biaxial case.

For the approximately uniaxial case, sample 1 shows a tendency for *a*-axis orientation along the machine direction (see Fig. 5). The *b* axes of this sample are almost perpendicular to the machine direction and are uniformly distributed between the transverse and thickness (ND) directions. With increasing drawdown the *a* axes are almost uniformly distributed around the machine direction, but exhibit maxima at about 47° (sample 2) to 61° (sample 3) away from the machine direction. The *b* axis remains at an angle of approximately 90° to the MD but slightly concentrates in the transverse direction. Generally the 200 and 020 pole figures indicate that samples 1–3 are nearly uniaxial in the machine direction. This is confirmed by the 110 pole figures.

For the samples with constant blowup ratio, the *b*-axis orientations are almost

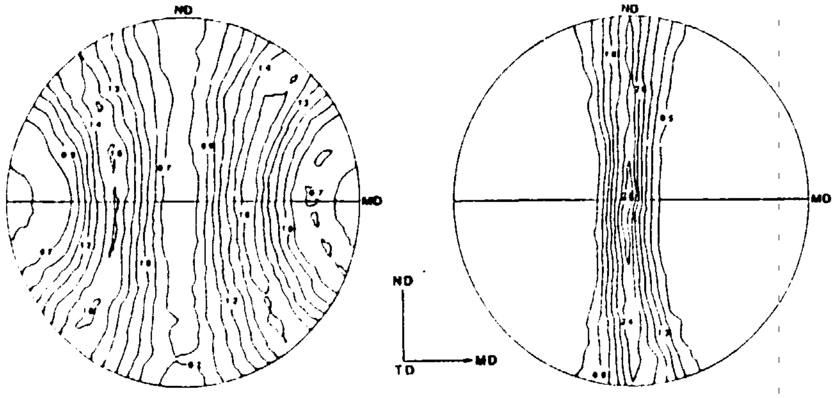

#3 - (200)   #3 - (020)

Fig. 6. Pole figures for (200) and (020) planes for film 3.

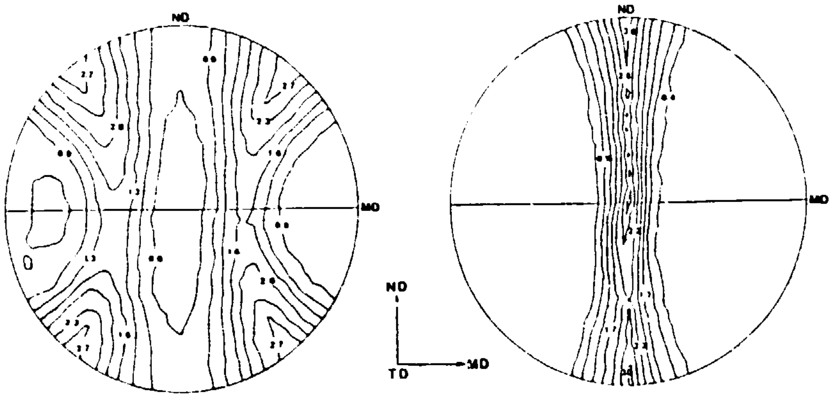

#6 - (200)

#6 - (020)

Fig. 7. Pole figures for (200) and (020) planes for film 6.

the same as those of the uniaxial samples 1–3 except that the *b* axis of sample 6 with the highest drawdown is slightly concentrated towards the film normal direction. The *a*-axis distribution shows slightly different behavior from that of the uniaxial case. The 200 pole figures of samples 4–6 show that the distributions for the *a* axis exhibit a maximum in each quadrant in the MD-ND plane. This maximum intensity concentration increases with increasing drawdown. The 110 pole figure confirms this tendency.

For the biaxial film (sample 8), the *a*-axis distribution also exhibits a maximum in the MD-ND plane in each quadrant, but is much weaker than for sample 6. There are greater intensities in areas of the 200 pole figure that are very weak for sample 6. A striking feature of Figure 8 is that the *b*-axis distribution is concentrated in the direction normal to the film.

Figure 9 shows the influence of processing conditions on small-angle x-ray scattering (SAXS) patterns taken with the beam normal to the plane of the film. For the uniaxial case, at low drawdowns (sample 1), a continuous ring with a maximum on the meridian is observed. With increasing drawdown, a distinctive two-point pattern develops. For the constant-blowup-ratio series, the SAXS

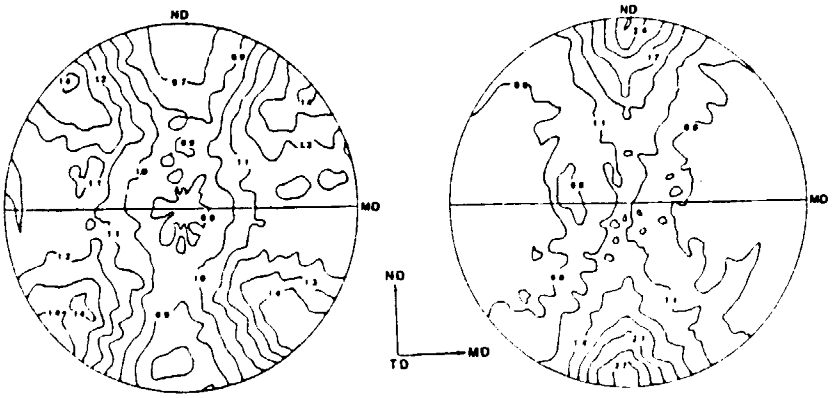

#8 - (200)

#8 - (020)

Fig. 8. Pole figures for (200) and (020) planes for film 8.

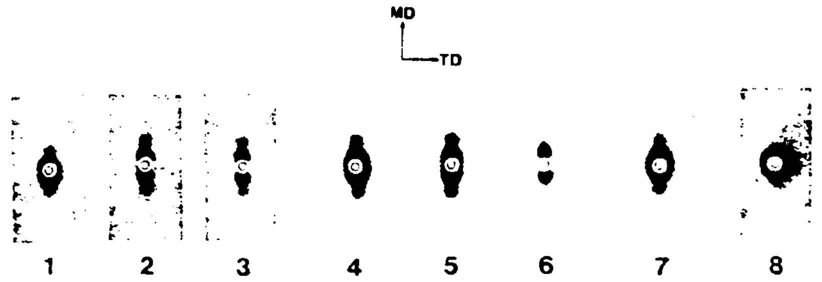

Fig. 9. SAXS patterns for films 1–8. The x-ray beam is normal to the film plane.

patterns are nearly the same as those of the uniaxial case but a little more dispersed around the beam stop.

For the biaxial films, the SAXS pattern exhibits two nearly uniform rings around the beam stop. These correspond to first- and second-order maxima. Three additional SAXS patterns were made of the biaxial sample with the x-ray beam parallel to MD, to TD, and at 45° to either MD or TD. All of these were "two-point" patterns. In each case the indicated periodicity was in the plane of the film, i.e., perpendicular to ND.

INTERPRETATION

Crystalline Orientation

The six quantities $\overline{\cos^2\Phi_{a1}}$, $\overline{\cos^2\Phi_{a2}}$, $\overline{\cos^2\Phi_{b1}}$, and $\overline{\cos^2\Phi_{b2}}$, $\overline{\cos^2\Phi_{c1}}$, and $\overline{\cos^2\Phi_{c2}}$ can be calculated from the pole-figure data. They can then be used to determine the White–Spruiell biaxial orientation factors for each of the three crystallographic axes. These results are summarized in Table IV.

For films 1–3, which should be approximately uniaxial,

$$f^B_{c1} > 0, \quad f^B_{c2} > 0 \tag{18a}$$

$$f^B_{a1} > 0, \quad f^B_{a2} < 0 \tag{18b}$$

$$f^B_{b1} < 0, \quad f^B_{b2} < 0 \tag{18c}$$

We plot the f^B_{a1}, f^B_{b1}, and f^B_{c1} as a function of drawdown for the uniaxial films in

TABLE IV
Orientation Factors and Crystallinity of Tubular Film

Samples	Fraction crystallinity X	Crystalline orientation factors f^B_{1a}	f^B_{1b}	f^B_{1c}	f^B_{2a}	f^B_{2b}	f^B_{2c}	Amorphous orientation factors f^B_1	f^B_2
1	0.726	0.198	−0.348	0.141	−0.053	−0.053	0.088	−0.49	−0.40
2	0.726	0.086	−0.435	0.348	−0.053	−0.035	0.088	−0.50	−0.37
3	0.720	0.002	−0.415	0.413	−0.033	−0.020	0.013	0.23	0.07
4	0.714	0.175	−0.399	0.224	−0.052	−0.042	0.094	−0.47	−0.34
5	0.707	0.081	−0.441	0.360	−0.071	−0.041	0.112	−0.43	−0.27
6	0.701	−0.009	−0.497	0.506	−0.118	−0.090	0.209	−0.45	−0.43
7	0.714	0.075	−0.396	0.321	−0.057	−0.065	0.123	−0.42	−0.15
8	0.701	0.012	−0.261	0.249	−0.050	−0.158	0.208	−0.02	−0.03

Figure 10. As drawdown increases f^B_{c1} increases; f^B_{b1} is negative and near −0.4; f^B_{a1} first increases, goes through a maximum, and then becomes negative. The f^B_{a1}, f^B_{b1}, f^B_{c1} plot resembles that of our earlier studies on polyethylene fibers.[19,20]

The data at constant blowup, samples 4–6, show

$$f^B_{c1} > 0, \quad f^B_{c2} > 0 \tag{19a}$$

$$f^B_{b1} < 0, \quad f^B_{b2} < 0 \tag{19b}$$

This is also true for sample 7. The constant-blowup-ratio data are also plotted in Figure 10. For film 8, which is more closely equal biaxial,

$$f^B_{c1} \approx f^B_{c2} \approx 0.22 \tag{20a}$$

$$f^B_{a1} \approx f^B_{a2} \approx -0.02 \tag{20b}$$

$$f^B_{b1} \approx f^B_{b2} \approx -0.2 \tag{20c}$$

These orientation factors are plotted as a White–Spruiell isosceles triangle diagram[35] in Figure 11. The general trend for either uniaxial or the constant

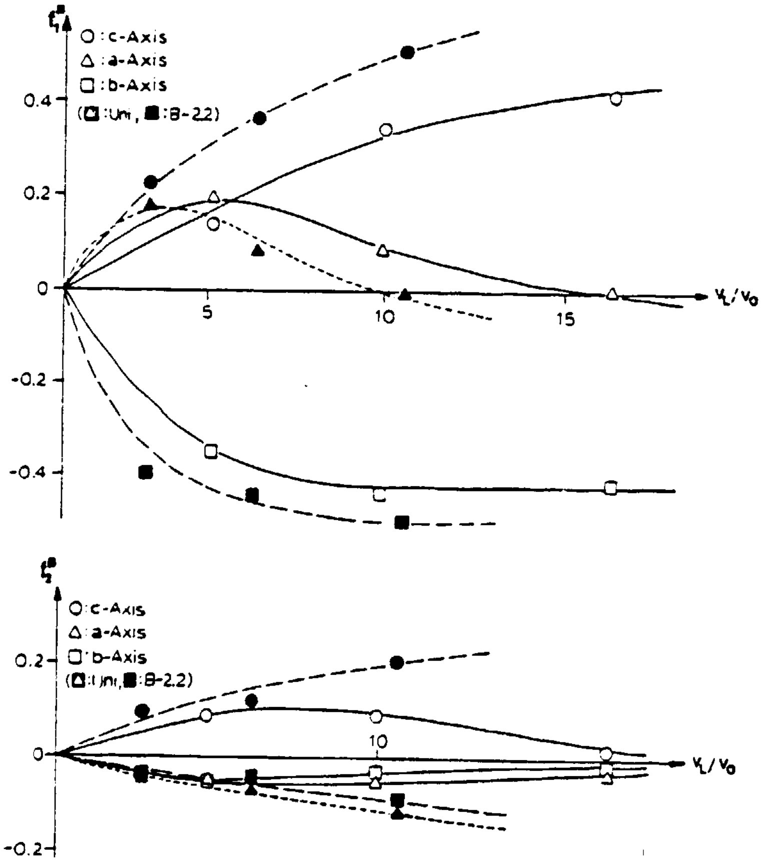

Fig. 10. Plot of crystalline orientation factors as a function of drawdown ratio: (a) f^B_{1a}, f^B_{1b}, f^B_{1c}; (b) f^B_{2a}, f^B_{2b}, f^B_{2c}.

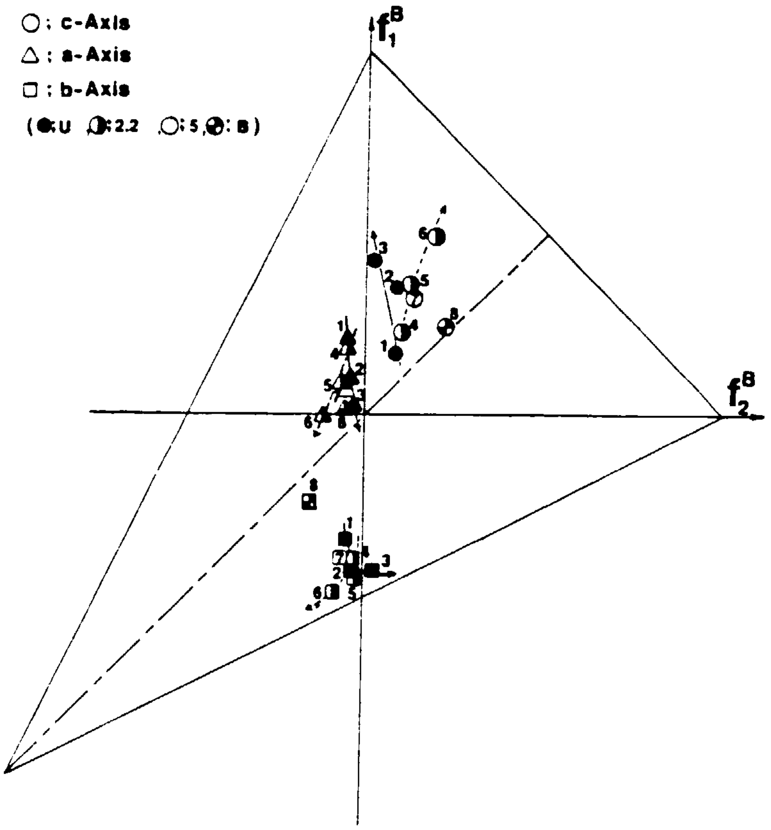

Fig. 11. Orientation triangle containing orientation factors for films produced in this research.

blowup series is toward increasing chain alignment in the machine direction with increasing drawdown. The orientation factors for sample 8 are nearly on the altitude, indicating equal biaxial orientation.

Crystalline Orientation-Stress Relation

In flowing polymer melts, the orientation factors are linearly related to the stress field through eq. (9c). The crystalline morphology of an oriented polymer should primarily depend upon the orientation of the melt prior to the onset of crystallization. This suggests

$$(f_{1j}^B - f_{2j}^B)_{\text{crys}} = G[(f_1^B - f_2^B)_{\text{melt}}] \tag{21}$$

where G is some unknown functional relation and j corresponds to the a, b, and c crystallographic axes. From eq. (21) it follows that

$$(f_{1j}^B - f_{2j}^B)_{\text{crys}} = G[(\sigma_1 - \sigma_2)_{\text{sol}}] \tag{22}$$

This suggests constructing a plot of

$$f_{1j}^B - f_{2j}^B \text{ vs. } F_L/2\pi R_L h_L - R_L \Delta p/h_L$$

This is shown in Figure 12.

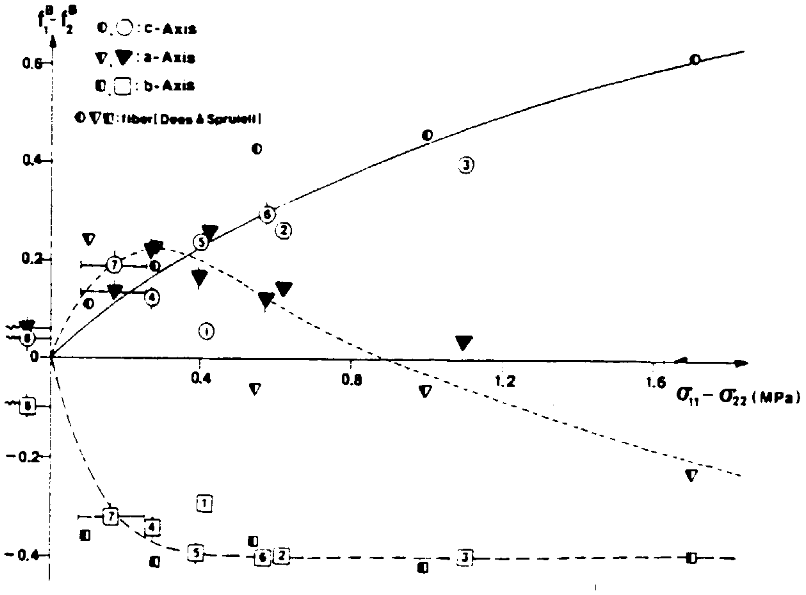

Fig. 12. Plot of difference in biaxial orientation factors $f_{1j} - f_{2j}$ as a function of $\sigma_1 - \sigma_2 = F_L/2\pi R h_L - R_L \Delta p/h_L$.

The trend of the $f_{1j}^B - f_{2j}^B$ vs. $\sigma_1 - \sigma_2$ plot is similar to that of the f_{1j}^B vs. V_L/V_0 data of Figure 10: $f_{1c}^B - f_{2c}^B$ increases with increasing $\sigma_1 - \sigma_2$, while $f_{1b}^B - f_{2b}^B$ is negative and about −0.4; $f_{1a}^B - f_{2a}^B$ increases, goes through a maximum, and then decreases, eventually becoming negative. In the plot of f_{1j}^B vs. V_L/V_0, different curves corresponding to different blowup ratios are obtained. The characteristics of Figure 12 are different. Within the range of experiments performed, all of the $f_{1j}^B - f_{2j}^B$ data points correlated with $\sigma_1 - \sigma_2$ independent of the blowup ratio.

Several years ago, Dees and Spruiell[19] found that they could correlate the Hermans–Stein uniaxial orientation factors for melt-spun polyethylene fibers with spin-line stress. For the case of uniaxial orientation, the difference $f_{1j}^B - f_{2j}^B$ reduces to the Hermans–Stein orientation factors. This suggests that we plot the data of Dees and Spruiell in Figure 12. We have done this and it is seen that the correlation is excellent. Melt-spun HDPE fibers obey the same crystalline orientation factor–stress relation as HDPE films.

Crystallinity

If we take the density of the perfect polyethylene crystal to be 1.002 and that of the amorphous regions to be 0.855, we obtain the fraction crystallinity X using eq. (15). This is tabulated in Table IV. The levels are of order 0.72.

It is of interest to note that both the measured densities and fractional crystallinities are higher than those found in earlier papers from our laboratories on melt-spun HDPE fibers.[19,20]

Birefringence

We now turn our attention to the interpretation of the birefringence data obtained on the films. Birefringence in HDPE films is primarily related to the orientation of polymer chains. As shown by White and Spruiell,[35] the birefringences Δn_{13} and Δn_{23} are related to the biaxial orientation factors through the relations

$$\Delta n_{13} = X(\Delta^{0c}_{ca} f^B_{1c} + \Delta^{0c}_{ba} f^B_{1b}) + (1 - X)\Delta^{0a} f^B_1 + (\Delta n_{13})_{\mathrm{form}} \qquad (23a)$$

$$\Delta n_{23} = X(\Delta^{0c}_{ca} f^B_{2c} + \Delta^{0c}_{ba} f^B_{2b}) + (1 - X)\Delta^{0a} f^B_2 + (\Delta n_{23})_{\mathrm{form}} \qquad (23b)$$

$$\Delta^{0c}_{ca} = n_c - n_a \qquad (24a)$$

$$\Delta^{0c}_{ba} = n_b - n_a \qquad (24b)$$

where n_c is the refractive index along the c crystallographic axis of a polyethylene single crystal, n_b the refractive index along the b crystallographic axis, and n_a along the a crystallographic axis. Δ^{0a} is the maximum (intrinsic) birefringence of the amorphous component and $(\Delta n_{13})_{\mathrm{form}}$ and $(\Delta n_{23})_{\mathrm{form}}$ are form birefringence due to the phase distribution. f^B_1 and f^B_2 are orientation factors for the amorphous regions.

As both Δn_{13} and Δn_{23} depend primarily upon f^B_{1j} and f^B_{2j} since X is a weak function of process conditions, we should expect that the birefringence should depend uniquely upon stress at crystallization. This is tested in Figure 13, where it is seen to correlate reasonably well.

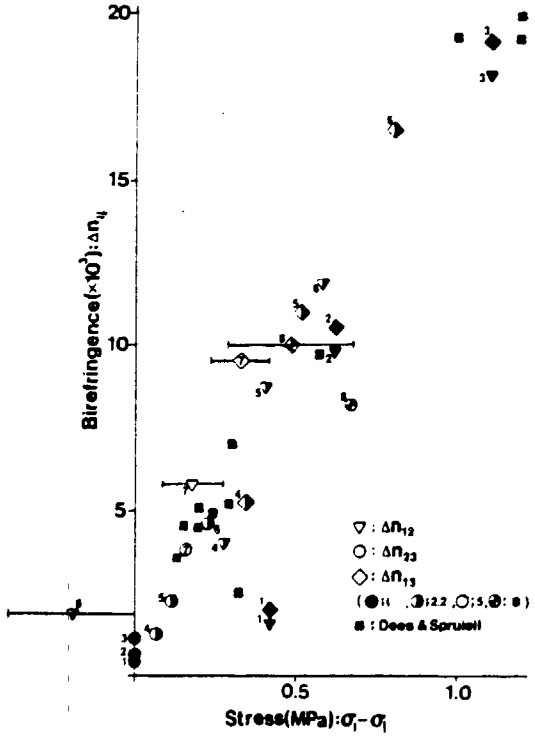

Fig. 13. Plot of birefringence Δn_{ij} as a function of stress $\sigma_i - \sigma_j$ at crystallization.

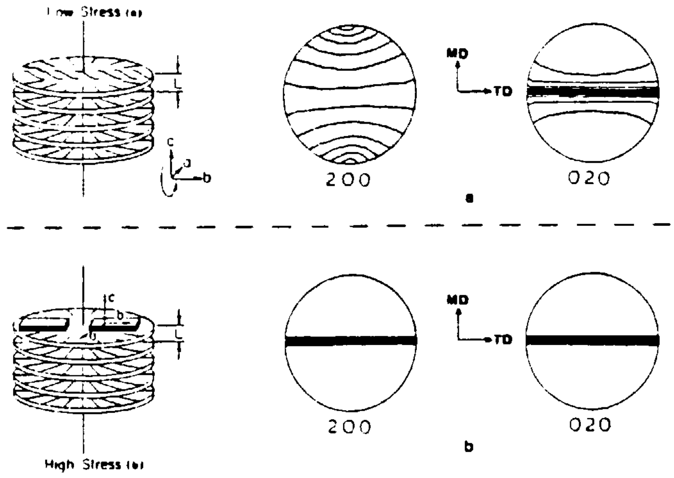

Fig. 14. Keller–Machin row structure (cylindrite model) for strictly uniaxial samples and the ideal pole figures consistent with "low" and "high" stress cases.

Dees and Spruiell[19] have correlated the birefringence of HDPE fibers with spin-line stress. We also plot their data in Figure 13. The agreement is strikingly good.

As discussed above, the molecular orientation and birefringence in the melt just prior to crystallization should be given by the rheo-optical law, eqs. (7) and (9). If there were no changes in orientation during crystallization, the plot shown in Figure 13 would be quite linear and its slope would equal the stress-optical coefficient of molten polyethylene at the temperature of crystallization. The functional relation shown in Figure 13 is approximately linear, but the slope of this line is much greater than the stress-optical coefficient of molten polyethylene. This demonstrates quite clearly the increase in orientation caused by crystallization. Such large increases in orientation during crystallization must be caused by a greater nucleation rate for nuclei having their chains oriented with respect to the applied fields, and the subsequent growth of these oriented nuclei.

It is possible to compute the amorphous orientation factors from eq. (23) if we know values for the crystalline orientation factors, crystallinity X, and the intrinsic birefringences. If we take the intrinsic birefringences Δ^{0c}_{ca}, Δ^{0c}_{ba}, and Δ^{0a} to be 0.058, 0.003, and 0.030, respectively, and use the previously calculated results for f^{B}_{1j}, f^{B}_{2j}, and X, we obtain the results listed in Table IV. The amorphous orientation factors especially at low values of the principal stresses at the freeze line are negative.

Negative uniaxial amorphous orientation factors have been reported by Nadella et al.[22] for polypropylene fibers melt spun at low drawdown stresses.

There is a significant lack of accuracy in the f^{B}_{1} and f^{B}_{2} data because of uncertainties in the experimental values of X, f^{B}_{1j}, f^{B}_{2j}, and, perhaps more importantly, in the intrinsic birefringence. Further, the contribution of form birefringence has been neglected. Thus the amorphous orientation results must be viewed with caution.

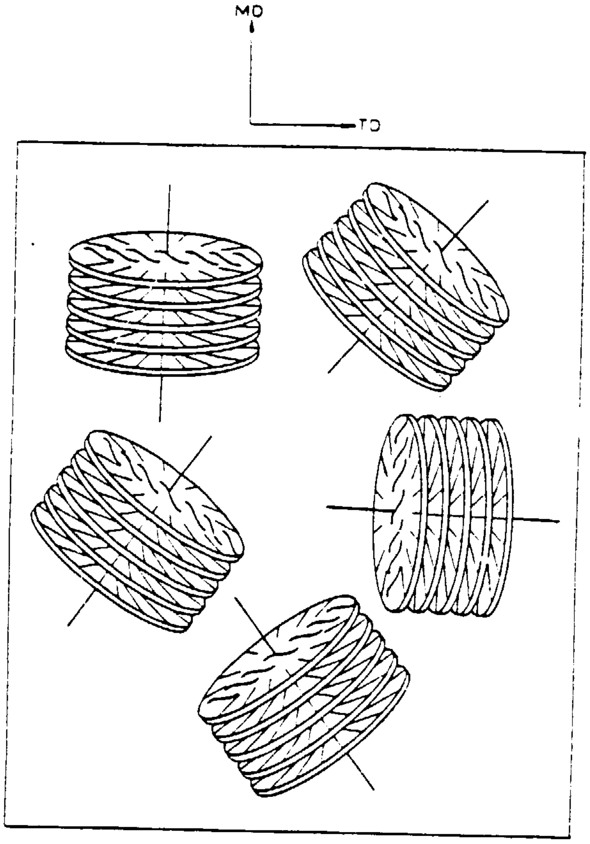

Fig. 15. Morphological model for film with equal biaxial orientation.

Proposed Morphology

We may couple our SAXS and orientation measurements to hypothesize a model for the crystalline morphology of the tubular films. The data for the uniaxial samples 1–3 indicate a row structure or cylindrite morphology of the type proposed by Keller and Machin.[58] The Keller–Machin model of row structure is illustrated in Figure 14 together with schematic pole figures consistent with the ideal row-structure models. It is to be noted that the twisted-lamellae structure of Figure 14(a) produces a 200 pole figure which exhibits a slight maximum at the MD. The schematic pole figures for this case are equivalent to the experimentally determined pole figures shown in Figure 5 for sample 1. The "high-stress" case shown schematically in Figure 14(b) is not achieved in any of the films produced in this research. The pole figures for samples 2 and 3 (see Fig. 6) appear to be intermediate between the two cases shown in Figure 14.

The samples with constant blowup ratio exhibit a slightly modified form of the row structure. The SAXS patterns indicate that the lamellae are still stacked primarily along the machine direction. In this form the orientation distribution is no longer uniaxial but exhibits a tendency for the *a* axis to concentrate somewhat in the MD-ND plane.

In the biaxially oriented sample 8 the morphology appears to be approximately equivalent to superimposed row structures as illustrated schematically in Figure 15. This morphology could be produced if the row nuclei are distributed in the plane of the film, depending on the relative stresses in the film at the freeze line. The morphology illustrated in Figure 15 is consistent with the "two-point" SAXS patterns observed when the x-ray beam is parallel to MD, to TD or at 45° to either MD or TD, as well as the pattern observed when the beam is parallel to ND (see Fig. 9). Furthermore, the 020 pole figure (Fig. 8) shows that the *b* axes tend to be perpendicular to both MD and TD (near ND) in this sample. The schematic arrangement shown in Figure 15 would produce a maximum in the 020 pole figure at the ND direction. This is the case because each "cylindrite" contains lamellae growing parallel to ND regardless of the orientation of the row nucleus in the plane of the film. These produce a concentration of axes near ND which does not occur in any other direction. It must be admitted that the schematic morphology shown in Figure 15 may not be the only possible morphology consistent with the data. It does, however, offer a reasonable interpretation of the data and provide an understanding of the effect of introducing a nonzero value of σ_2.

The research described here was supported in part by the National Science Foundation through NSF Grant Eng. 78-21889.

References

1. D. R. Holmes and R. P. Palmer, *J. Polym. Sci.*, **31**, 345 (1958).
2. P. H. Lindenmeyer and S. Lustig, *J. Appl. Polym. Sci.*, **9**, 227 (1965).
3. C. R. Desper, *J. Appl. Polym. Sci.*, **13**, 169 (1969).
4. L. E. Dowd, *SPE J.*, **28**, 22 (1972).
5. G. Menges and W. Predohl, *Plastverarbeiter*, **23**, 338 (1972).
6. T. Nagasawa, T. Matsumura, S. Hoshino, and K. Kobayoshi, *Appl. Polym. Symp.*, **20**, 275 (1973).
7. W. Ast, *Kunststoffe*, **63**, 427 (1973); **64**, 146 (1974).
8. C. D. Han and J. Y. Park, *J. Appl. Polym. Sci.*, **19**, 3275 (1975).
9. C. D. Han and R. Shetty, *IEC Fund*, **16**, 49 (1977).
10. W. F. Maddams and J. E. Preedy, *J. Appl. Polym. Sci.*, **22**, 2721 (1978).
11. W. F. Maddams and J. E. Preedy, *J. Appl. Polym. Sci.*, **22**, 2739 (1978).
12. W. F. Maddams and J. E. Preedy, *J. Apply. Polym. Sci.*, **22**, 2751 (1978).
13. W. F. Maddams and J. R. Preedy, *J. Appl. Polym. Sci.*, **22**, 3027 (1978).
14. K. Oda, J. L. White, and E. S. Clark, *Polym. Eng. Sci.*, **18**, 53 (1978).
15. W. Dietz, J. L. White, and E. S. Clark, *Polym. Eng. Sci.*, **18**, 273 (1978); *Rheol. Acta*, **17**, 676 (1978).
16. J. L. White and W. Dietz, *Polym. Eng. Sci.*, **19**, 1081 (1979).
17. J. L. White and W. Dietz, *J. Non Newt. Fluid Mech.*, **4**, 299 (1979).
18. K. Choi, J. L. White, and J. E. Spruiell, *J. Appl. Polym. Sci.*, **25**, 2777 (1980).
19. J. R. Dees and J. E. Spruiell, *J. Appl. Polym. Sci.*, **18**, 1053 (1974).
20. J. L. White, K. L. Dharod, and E. S. Clark, *J. Appl. Polym. Sci.*, **18**, 2539 (1974).
21. J. E. Spruiell and J. L. White, *Polym. Eng. Sci.*, **15**, 666 (1975).
22. H. P. Nadella, H. M. Henson, J. E. Spruiell, and J. L. White, *J. Appl. Polym. Sci.*, **21**, 3003 (1977).
23. C. L. Rohn, *J. Polym. Sci.*, **46C**, 161 (1974).
24. Z. W. Wilchinsky, *J. Appl. Polym. Sci.*, **7**, 923 (1963).
25. C. R. Desper and R. S. Stein, *J. Appl. Phys.*, **37**, 3990 (1966).
26. L. E. Alexander, *X-Ray Diffraction Methods in Polymer Science*, Wiley, New York, 1969.
27. P. H. Hermans and P. Platzek, *Kolloid Z.*, **88**, 68 (1939).
28. J. J. Hermans, P. H. Hermans, D. Vermaas, and A. Weidinger, *Rec. Trav. Chim. Pays-Bas*, **65**, 427 (1946).

29. P. H. Hermans, J. J. Hermans, D. Vermaas, and A. Weidinger, *J. Polym. Sci.*, **3**, 1 (1947).
30. R. S. Stein, *J. Polym. Sci*, **31**, 335 (1958).
31. S. Nomura, H. Kawai, I. Kimura, and M. Kagiyama, *J. Polym. Sci.* A-2, **5**, 479 (1967).
32. H. Kawai, in *Proceedings, Fifth International Rheology Congress*, 1969, Vol. 1, p. 97.
33. S. Nomura, H. Kawai, I. Kimura, and M. Kagiyama, *J. Polym. Sci.* A-2, **8**, 383 (1970).
34. S. Nomura, N. Nakamura, and H. Kawai, *J. Polym. Sci.* A-2, **9**, 407 (1971).
35. J. L. White and J. E. Spruiell, *Polym. Eng. Sci.*, to appear.
36. K. Matsumoto, J. F. Fellers, and J. L. White, *J. Appl. Polym. Sci.*, **26**, 85 (1981).
37. A. S. Lodge, *Trans. Faraday Soc.*, **52**, 120 (1956).
38. H. Janeschitz-Kriegl; *Adv. Polym. Sci.*, **6**, 170 (1969).
39. J. L. S. Wales, *Rheol. Acta*, **8**, 38 (1969).
40. J. L. S. Wales and W. Philippoff, *Rheol. Acta*, **12**, 25 (1973).
41. C. D. Han and L. H. Drexler, *J. Appl. Polym. Sci.*, **17**, 2329 (1973).
42. F. H. Gortemaker, M. C. Hanson, B. DeCindio, H. M. Laun, and H. Janeschitz-Kriegl, *Rheol. Acta*, **15**, 256 (1976).
43. I. Hamana, M. Matsui, and S. Kato, *Melliand Textilber.*, **4**, 382 (1969).
44. M. A. A. Omotoso, J. L. White, and J. F. Fellers, *J. Appl. Polym. Sci.*, **25**, 1573 (1980).
45. L. S. Thomas and K. Cleereman, *SPE J.*, **28**, 61 (1972).
46. T. Alfrey, *SPE Trans.*, **5**, 68 (1965).
47. J. R. A. Pearson and C. J. S. Petrie, *J. Fluid Mech.*, **40**, 1 (1970).
48. J. R. A. Pearson and C. J. S. Petrie, *J. Fluid Mech.*, **42**, 609 (1970).
49. J. R. A. Pearson and C. J. S. Petrie, *Plast. Polym.*, **38**, 85 (1970).
50. R. Farber and J. M. Dealy, *Polym. Eng. Sci.*, **14**, 435 (1974).
51. W. Flugge, *Stresses in Shells*, Springer, Berlin, 1960.
52. M. H. Wagner, *Rheol. Acta*, **15**, 40 (1976).
53. R. S. Stein, *J. Polym. Sci.*, **24**, 383 (1957).
54. C. J. Heffelfinger and R. L. Burton, *J. Polym. Sci.*, **47**, 289 (1960).
55. J. B. Nichols, *J. Appl. Phys.*, **25**, 840 (1954).
56. S. L. Aggarwal and G. P. Tilley, *J. Polym. Sci.*, **18**, 17 (1955).
57. Z. W. Wilchinsky, in *Advances in X-Ray Analysis*, Plenum, New York, 1963, Vol. 6, p. 231.
58. A. Keller and M. J. Machin, *J. Macromol. Sci. Phys.*, **B1**, 41 (1967).

Received February 10, 1981
Accepted June 23, 1981

Appendix C

An Investigation of Optical Clarity and Crystalline Orientation in Polyethylene Tubular Film

HIROSHI ASHIZAWA

Nissan Petrochemical, Chiba, Japan

JOSEPH E. SPRUIELL

Polymer Engineering
University of Tennessee
Knoxville, Tennessee 37996

and

JAMES L. WHITE

Polymer Engineering Center,
University of Akron,
Akron, Ohio 44325

A study of the crystalline orientation, light transmission, and surface roughness of polyethylene tubular film prepared in our laboratories is presented. The present studies were primarily carried out on low-density (LDPE) and linear-low-density (LLDPE) polyethylene films. The optical properties of a few films of high-density polyethylene (HDPE) prepared for a previous study of morphology were characterized for comparison to the LDPE and LLDPE films. Wide angle X-ray diffraction and birefringence were used to characterize orientation. Both the LDPE and LLDPE films exhibited crystalline texture in which the *b*-axes tended to be perpendicular to the film surface and the *a*-axes had some tendency to align with the machine direction. The *c*-axes tended to be concentrated in the plane of the film with nearly equal biaxial orientation with respect to the machine and transverse directions. Little variation in the crystalline orientation was found with changes of process conditions in the range studied. Birefringence results indicate that the amorphous regions developed an orientation in which the chains tend to be normal to the film surface. The majority of light scattering from these films and a series of HDPE films was from the surface and not from the film interior. The transmission coefficient for the surface contribution was found to be a monotonic decreasing function of the standard deviation of the surface height obtained from surface profiles measured by profilometer. The surface asperites were largest for the HDPE and smallest for the LDPE samples. The intensity of both the surface and interior contributions to the scattering increased with increasing frostline height, i.e., a slower cooling rate. As draw-down ratio and blow-up ratio increase the scattering contribution from the film interior decreases but the contribution from the surface increases somewhat. These effects are discussed in terms of the changes in crystalline morphology and surface roughness produced by flow defects generated during extrusion.

INTRODUCTION

Tubular film extrusion is one of the most important of polymer-processing operations. There has, however, been little study of this operation, especially with regard to structure development and optical characteristics of films produced in the tubular blowing operation. Various investigators

(1–5) have considered the optical clarity and haze of tubular film. It was recognized by Huck and Clegg (2) in 1961 that the light scattering originates from both surface irregularities and bulk scattering and that the former is predominant. They did not distinguish the relative amounts of surface and bulk scattering. Procedures have become available for accomplishing this (6). Such data treatment is described by Stehling, *et al.* (5) for a series of low-density polyethylenes (LDPE). They correlate the surface haze with scanning electron microscopy observations of the surface roughness of films. Investigations of polymer chain and crystalline orientation in extruded tubular film have been published from several laboratories (7–18). These, studies have related the internal structure of low-density polyethylene (7–9), high-density polyethylene (10–14, 16), polystyrene (15), nylon-6 (10), polypropylene (17), polybutene-1 (4, 10), and polyethylene-polypropylene blends (18). Several of these investigations have sought to relate orientation and crystalline morphology to process conditions (12–18). However, none of these researches involves studies of both crystalline orientation and optical characteristics of films.

In the present paper, we describe an experimental study of the optical clarity and crystalline orientation of a series of tubular films from varying types of polyethylenes. We make a comparative study of representative low-density (LDPE) and linear-low-density (LLDPE) as a function of process conditions. Some comparisons to high-density-polyethylene (HDPE) films are also made. This paper represents a continuation of our earlier investigations of tubular film extrusion (15–19).

EXPERIMENTAL

Materials

The polymers which were studied in this investigation were a commercial LDPE, LLDPE, and HDPE. The characteristics of these polymers are summarized in *Table 1*.

Film Preparation

The tubular film was produced with a ¾-inch Raineville screw extruder with an annular blown film die (inside diameter of 1.496 cm and outside diameter 1.605 cm). The extrusion temperature was 180°C. Eleven LDPE and L-LDPE films were prepared and two HDPE films were prepared according to the conditions outlined in *Table 2*.

Density and Crystyallinity Measurements

The densities of the films were determined at 23°C using a distilled water-isopropyl alcohol density gradient column. The crystalline fraction was obtained through

$$X = \frac{\rho_c(\rho - \rho_a)}{\rho(\rho_c - \rho_a)} \qquad (1)$$

where ρ_c, the crystalline density of polyethylene, was taken as 1.002 and ρ_a, the amorphous density, as 0.855. ρ is the sample density.

Table 1. Characteristics of polyethylenes investigated in this study.

Polymer	Source	Density	Melt index
LDPE	Union Carbide	0.918	1.0
LLDPE	Union Carbide	0.921	2.0
HDPE	Chemplex	0.96	0.98

Table 2. Conditions for formation of tubular film.

Designation	Material	Draw-down ratio (V_L/V_o)	Blowup ratio B	Frostline height (cm)	Thickness (μm)
L1	LDPE	4.0	3.5	12	38.1
L2		4.0	3.5	9	48.3
L3		4.0	3.5	6	44.5
L4		4.0	3.5	2.5	44.5
L5		1.0	2.5	9	208.3
L6		2.0	2.5	9	114.3
L7		4.0	2.5	9	53.3
L8		6.0	2.5	9	33.0
L9		8.0	2.5	9	26.7
L10		4.0	1.0	9	147.3
L11		4.0	4.5	9	22.9
LL1	LLDPE	4.0	3.5	12	31.8
LL2		4.0	3.5	9	33.0
LL3		4.0	3.5	6	36.8
LL4		4.0	3.5	2.5	34.3
LL5		1.0	2.5	9	241.3
LL6		2.0	2.5	9	95.3
LL7		4.0	2.5	9	47.0
LL8		6.0	2.5	9	36.8
LL9		8.0	2.5	9	30.5
LL10		4.0	1.0	9	112.0
LL11	HDPE	4.0	4.5	9	22.9
H4		3.4	2.2	15	45.7
H6		10.6	2.3	15	14.0

Characterization of Orientation

Orientation was studied by wide-angle X-ray diffraction and birefringence techniques. Pole figures for the 200, 020, and 110 reflections of polyethylene were determined by procedures in previous publications (16, 17, 20). A General Electric X-ray diffractometer equipped with a single crystal orienter was used. The radiation used was CuKα of wavelength 1.542 Å. The X-ray unit was operated at 40 KV and 15 mA.

The orientation of the crystallographic axes in terms of the machine and transverse directions was expressed through the orientation factors (15–20)

$$f_{1j}^{B} = 2\,\overline{\cos^2\Phi_{1j}} + \overline{\cos^2\Phi_{2j}} - 1 \qquad (2a)$$

$$f_{2j}^{B} = 2\,\overline{\cos^2\Phi_{2j}} + \overline{\cos^2\Phi_{1j}} - 1 \qquad (2b)$$

Here '1' is the machine direction, '2', is the transverse direction and j represents the a, b, or c crystallographic axes. The $\overline{\cos^2\Phi_{1j}}$, $\overline{\cos^2\Phi_{2j}}$ were determined from the 200 and 110 reflections using a treatment equivalent to that of Stein (21).

In-plane and out-of-plane birefringences were measured using an optical bench with a mounted goniometer. This is equivalent to an apparatus developed by Stein (22) which has been applied extensively in our own laboratories (15–17).

Direct Transmission Factor Measurements

The clarity of the films was evaluated by measuring the direct transmission of light through the films. Since light that is not transmitted is scattered, the scattered light can be obtained by difference. The direct optical transmission factor was measured using a wide-angle light-scattering apparatus (G. N. Wood Model 600 monophotometer). A source of monochromatic light of wavelength 5460 Å was used.

The direct transmission factor is defined as the ratio of the intensity of the beam transmitted through the sample to the intensity incident on the sample. The total direct transmission factor, T, is the product of a "surface phase" direct transmission factor, T_S, and a "bulk phase" direct transmission factor, T_B; i.e.,

$$T = T_S T_B \tag{3}$$

The direct transmission factor of the bulk or interior phase, T_B, was evaluated independent of T by dipping the film into glycerin, which has nearly the same index of refraction as the polyethylene film ($n = 1.47$). This eliminates the scattering from the rough surface of the film. A pair of glass slides was used to hold the film and liquid. T_S was evaluated from the measured values of T and T_B through *Eq* 3. The turbidity, τ, of the bulk phase was also calculated using

$$T_B = \exp(-\tau t) \tag{4}$$

where t is the film thickness. This method of separating the surface and bulk transmission factors is due to Clampitt, *et al.* (6).

Scanning Electron Microscopy

The surface textures of the films were examined using a scanning electron microscope (AMR Model 900). The films were coated with gold-palladium in a vacuum chamber to eliminate charging.

Surface Profile Measurement

A profile of the surface roughness of each tubular blown film was obtained using a Tencor Alpha-Step 100 surface profiler. The radius of the diamond stylus used in this experiment was about 2 μm and the stylus loading was adjusted to about 3 mg to produce good contact with the polyethylene film surfaces. The total possible stylus travel across the sample is 3 mm, but 0.4 mm long scans were generally used for the surface statistics.

A least squared line was calculated for each 0.1 mm long scan to eliminate the effects of large bumps as well as instrument drift. These sets of least square lines were considered as the mean surface level and differences were considered to be the basic profile $h(x)$. The standard deviation of the height was calculated from

$$\sigma = \left[\frac{1}{L}\int_0^L h^2(x)dx\right]^{1/2} \tag{5}$$

$$= \left[\frac{1}{N}\sum_{n=1}^{N} h^2(n)\right]^{1/2} \tag{6}$$

RESULTS

Crystallinity and Orientation

Structural studies of the HDPE samples were reported and discussed previously (16). We concentrate here on the characterization of the LDPE and LLDPE films. The densities of the LDPE films are in the range 0.920 to 0.921 and for the LLDPE films in the range 0.917 to 0.919. These values correspond to crystallinities of 48.2 to 48.7 percent for LDPE and 46.1 to 47.5 percent for LLDPE. For reference, the crystallinities of the HDPE samples were 70.1 to 71.4 percent.

Typical pole figures for the 200 and 020 reflections are presented in *Figs. 1* and *2*. The results for all of the LDPE and LLDPE films were generally similar. The *a* crystallographic axis tends to lie in the plane of the film but with a higher concentration in the machine direction. The *b*-axis tends to lie in the plane perpendicular to the machine direction with a higher concentration in the normal direction. The latter effect is more pronounced for the LDPE films, with the LLDPE films exhibiting a more uniform (uniaxial) distribution of the *b* axes about the machine direction.

The birefringences of the LDPE and LLDPE films are summarized in *Table 3*. Typical variations with processing conditions are shown plotted in *Fig. 3*. The magnitudes for all the birefringences are relatively small. Generally $\Delta n_{13} > \Delta n_{23}$, indicating a slightly greater tendency for the chains to align parallel to the machine direction than the transverse direction.

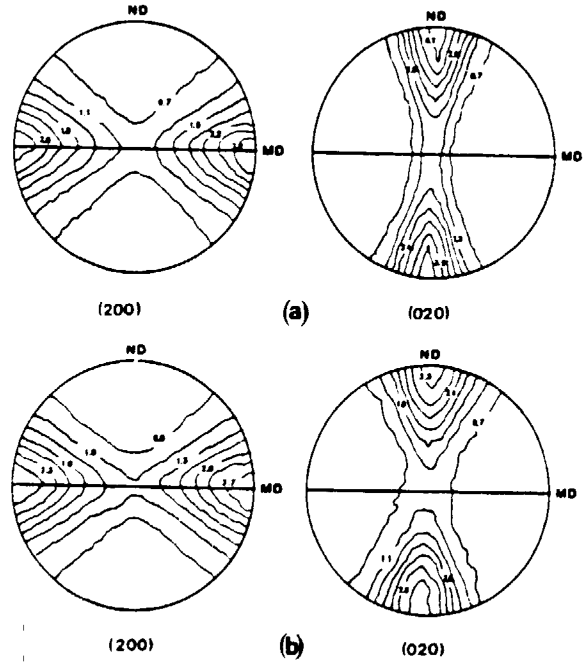

Fig. 1. 200 and 020 pole figures for LDPE films. (a) L-9 v_L/v_o = 8.0, B = 2.5 (b) L-11 v_L/v_o = 4.0, B = 4.5

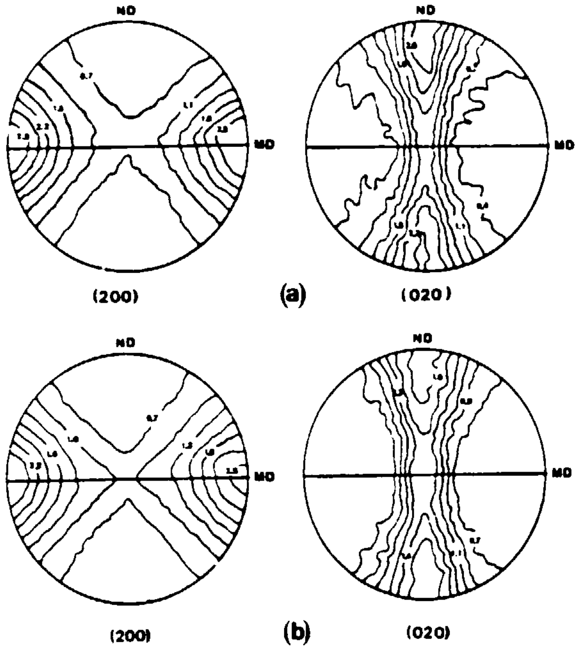

Fig. 2. 200 and 020 pole figures for LLDPE films. (a) LL-9 $v_L/v_o = 8.0$, $B = 2.5$ (b) LL-11 $v_L/v_o = 4.0$, $B = 4.5$

Table 3. Birefringences of polyethylene films.

Sample	$\Delta n_{13} \times 10^4$	$\Delta n_{23} \times 10^4$	$\Delta n_{12} \times 10^4$
L-2	6.95	7.73	−0.73
L-6	5.65	4.16	1.49
L-7	6.95	6.81	0.13
L-8	9.65	7.90	1.75
L-9	9.60	8.57	1.03
L-10	10.8	1.63	9.13
L-11	10.9	7.48	3.42
LL-2	6.49	4.58	1.90
LL-6	3.78	1.20	2.58
LL-7	7.50	3.20	4.30
LL-8	8.38	4.70	3.68
LL-9	9.13	5.04	4.09
LL-10	11.6	1.13	10.5
LL-11	6.60	5.32	1.36

Consider films L6–L9 and LL6–LL9. As drawdown ratio increases, the magnitude of both Δn_{13} and Δn_{23} increase. (See *Fig. 3a.*) Inspection of the Δn_{12} data show that for the LDPE

$$\Delta n_{23} > \Delta n_{12} \tag{8a}$$

but for the LLDPE

$$\Delta n_{23} \sim \Delta n_{12} \tag{8b}$$

With increasing blowup ratio (see *Fig. 3b*), Δn_{13} and Δn_{12} decrease and Δn_{23} increases. As the blowup ratio approaches the drawdown ratio, Δn_{12} tends toward zero.

The biaxial crystalline orientation factors determined from the pole figures are plotted in an orientation function triangle diagram in *Fig. 4* and tabulated in *Table 4*. There is little difference in the crystalline orientations of any of the samples. The effect of changing the process variables within the range studied is small.

Amorphous orientation factors were calculated from birefringence data in the manner proposed by White and Spruiell (20) with form birefringence neglected. The results are summarized in *Table 4*. Both f_1^B and f_2^B are negative, suggesting that the chains in the amorphous regions tend to be normal to the surface of the film. This is most pronounced in the LDPE.

Optical Clarity and Direct Transmission Factors

Direct transmission factors and turbidities of LDPE, LLDPE, and HDPE films were measured. As the films have varying thicknesses, we have computed turbidities for all of the films investigated using *Eq 4*. Data for T, T_B, T_S, and τ for all of the films investigated are summarized in *Table 5*. Values of T and T_S are smaller and τ is largest for the HDPE films. The values of T and T_S are the largest and τ the smallest for the LDPE films. The values of T_S in general are much smaller than T_B and are closer to T, indicating that surface scattering is dominant in films having thicknesses in the range studied in this investigation. Values of T_B are in the range of 0.85 to 0.95 while T_S has values of order 0.85 for the LDPE, 0.7 to 0.8 for LLDPE, and 0.45 for HDPE.

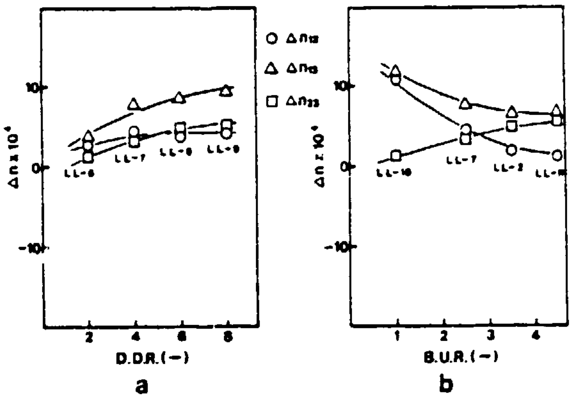

Fig. 3. Birefringences of L-LDPE films as a function of process conditions. a) Δn_{ij} vs drawdown ratio v_L/v_o with $B = 2.5$ and frostline height of 9 cm. b) Δn_{ij} vs blowup ratio with drawdown ration of 4.0 and frostline height of 9 cm.

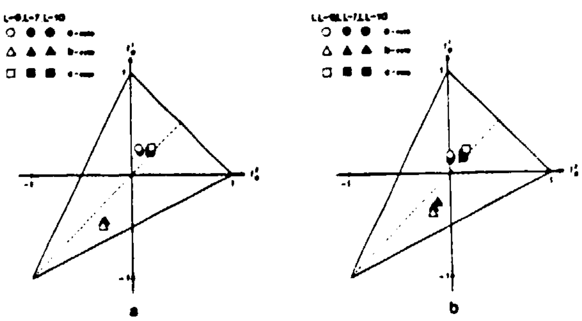

Fig. 4. Orientation triangles presenting data for f^B_{aj}, f^B_{bj}, f^B_{cj} of: (a) LDPE Films (b) LLDPE films.

Table 4. Orientation factors for polyethylene.

Sample Number	Crystalline orientation factors						Amorphous orientation factors	
	f^B_{1a}	f^B_{2a}	f^B_{1b}	f^B_{2b}	f^B_{1c}	f^B_{2c}	f^B_1	f^B_2
L-7	0.223	0.080	−0.452	−0.270	0.229	0.190	−0.33	−0.28
L-9	0.253	0.072	−0.500	−0.276	0.252	0.205	−0.35	−0.29
L-11	0.239	0.081	−0.468	−0.282	0.229	0.201	−0.34	−0.29
LL-7	0.135	−0.003	−0.291	−0.132	0.157	0.135	−0.20	−0.20
LL-9	0.170	0.004	−0.397	−0.174	0.227	0.170	−0.29	−0.24
LL-11	0.162	0.018	−0.345	−0.165	0.184	0.147	−0.25	−0.21

Table 5. Direct transmission factors and turbidity of tubular film.

Sample designation	Transmission Factors × 100			
	T	T_s	T_B	$\tau(cm^{-1})$
L2	81.1	85.8	94.5	11.7
L3	82.3	84.7	97.1	6.5
L4	83.6	86.6	96.5	8.0
L5	64.8	87.0	72.8	15.3
L6	75.9	89.1	85.2	14.1
L7	82.3	85.8	95.8	8.0
L8	84.2	86.9	96.9	9.5
L9	86.2	88.3	97.5	9.3
L10	80.0	91.1	87.8	8.8
L11	83.7	85.4	98.0	8.6
LL1	67.4	71.2	94.8	16.9
LL2	69.0	72.4	95.3	14.5
LL5	48.0	81.0	89.3	21.7
LL6	66.4	80.8	82.2	20.5
LL7	70.7	75.1	94.1	12.9
LL8	73.5	76.7	95.9	11.4
LL9	73.1	75.1	97.3	9.0
LL10	68.3	80.5	84.8	14.8
LL11	72.2	74.6	96.8	14.2
H4	39.21	45.6	85.9	33.3
H6	39.6	41.3	95.9	29.8

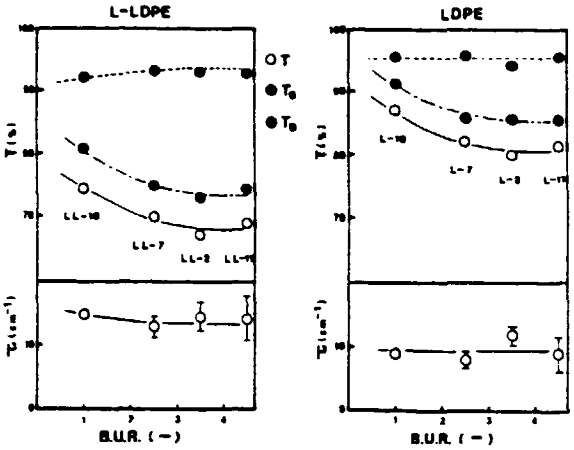

Fig. 6. Transmissivities T, T_s, and T_B (normalized to film thickness of 54 μm) and turbidity as a function of blowup ratio: (a) LLDPE (b) LDPE

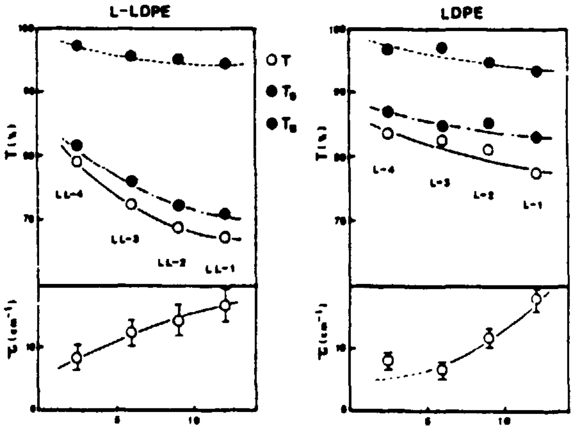

Fig. 7. Transmissivities T, T_s, and T_B (normalized to film thickness of 54 μm) and turbidity as a function of frostline height: (a) LLDPE (b) LDPE

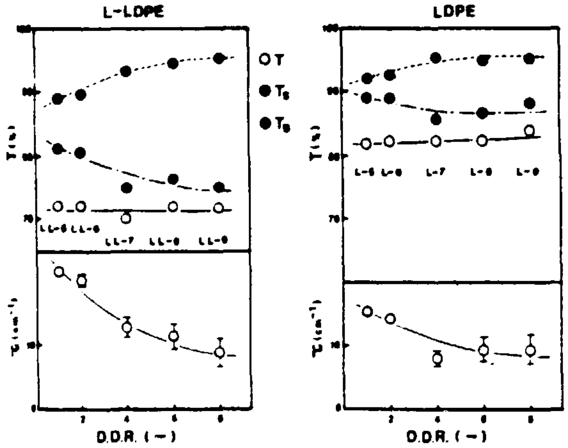

Fig. 5. Transmissivities T, T_s, and T_B (normalized to film thickness of 54 μm) and turbidity as a function of drawdown ratio: (a) LLDPE (b) LDPE

The influence of process variables on the transmissivities T, T_S, and T_B and the turbidity is shown in *Figs. 5-7*. The values of T_B were normalized to a film thickness of 54 μm in these calculations. For both the LDPE and LLDPE, T_B increases (τ decreases) with V_L/V_o at constant blowup ratio and frostline height, while T_s decreases (*Fig. 5*). These balance, giving approximately the same T. The effect of blowup ratio on T, T_s, normalized T_B, and τ is shown in *Fig. 7*. For both LDPE and LLDPE, T_B and τ are independent of blowup ratio, at fixed V_L/V_o and frostline height. The effect of increasing frostline height at fixed drawdown ratio V_L/V_o and blowup rato is shown in *Fig. 7*. T_S and the normalized T_B both decrease while τ increases.

Surface Roughness

It is clear from the data of *Table 5* and *Figs. 5–7* that scattering by the surfaces of the film is a primary reason for the reduction in light transmission through films. It is reasonable to hypothesize that a primary reason for these surface scattering characteristics should be the roughness of the surface. This is supported by experimental studies of Stehling, *et al.* (6), who find that scattering from the surface of polyethylene films correlates with surface roughness observed in SEM photomicrographs.

Typical SEM photomicrographs of our samples of blown LDPE, LLDPE, and HDPE films are shown in *Fig. 8*. It is clear that HDPE has the roughest surface. The surface of the LLDPE is rougher than that of the LDPE.

Surface profiles were measured on several LDPE (L-2, L-3, L-4), LLDPE (LL-2, LL-3, LL-4), and HDPE (H4, H6) films. Typical surface profiles are shown in *Fig. 9*. HDPE films have a much rougher surface than LLDPE and LDPE. The standard deviations of the height σ are summarized in *Table 6*. HDPE films have about five times larger values of σ than LLDPE and ten times larger than LDPE. Typical histograms of height distribution generated from surface profile data are shown in *Fig. 10*. The curves are Gaussian in character.

Table 6. Surface roughness of polyethylene film.

Sample	Material	Scan Direction	σ, μm
L-2	LDPE	MD	0.020
		TD	0.020
L-3		MD	0.022
		TD	0.021
L-4		MD	0.016
		TD	0.016
LL-2	LLDPE	MD	0.043
		TD	0.050
LL-3		MD	0.039
LL-4		TD	0.046
		MD	0.028
		TD	0.032
4	HDPE	MD	0.206
		TD	0.205
6		MD	0.127
		TD	0.197

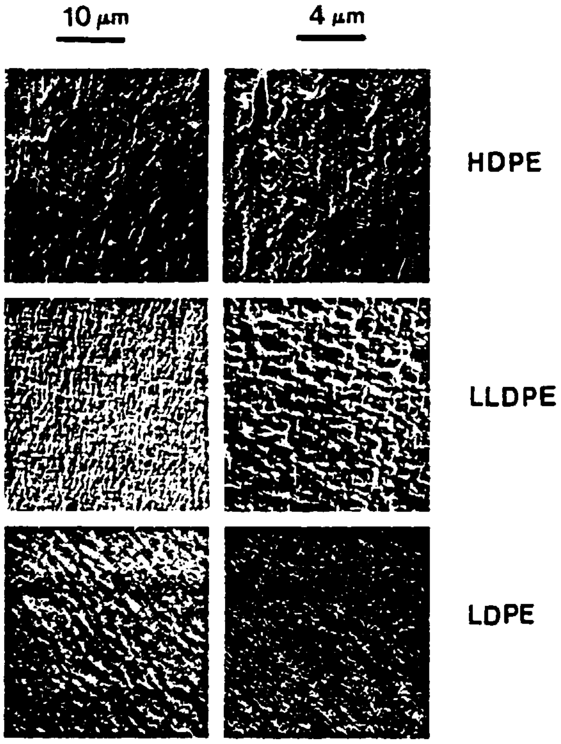

Fig. 8. SEM photomicrographs of typical film surfaces.

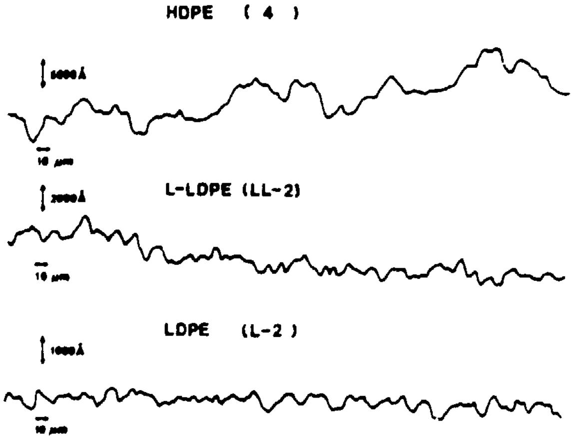

Fig. 9. Typical surface roughness profiles.

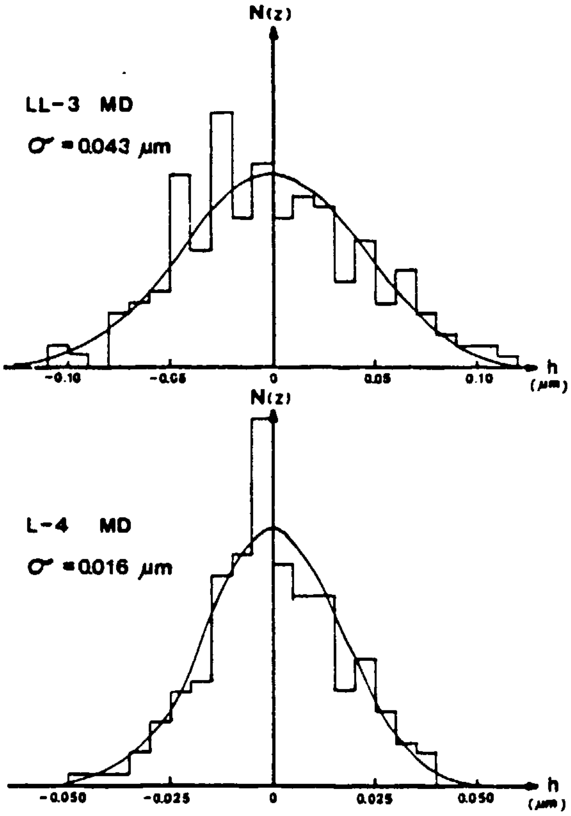

Fig. 10. Typical histograms of asperite height distribution.

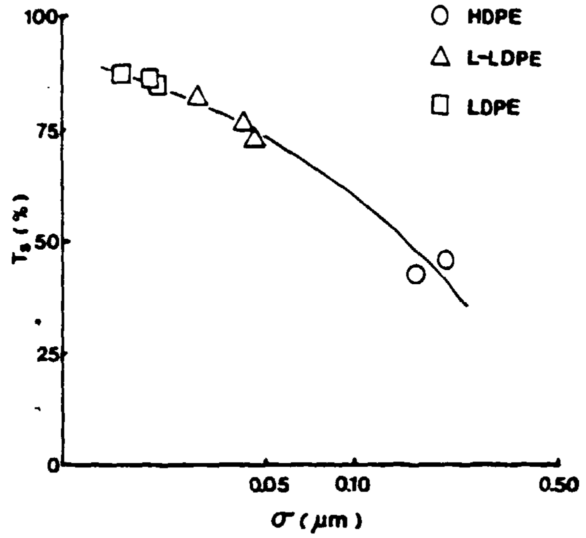

Fig. 11. Surface transmissivity as a function of standard deviation of roughness (mean asperite height).

In *Fig. 11*, we plot the surface transmission factor T_S as a function of the standard deviation σ of the surface roughness. LDPE, LLDPE, and HDPE data are included in the plot. We find that T_S is a monotonic decreasing function of σ.

DISCUSSION

Interpretation of Orientation

Biaxial orientation factors for the crystalline regions plotted in *Fig. 4* indicate that our sample of LDPE has slightly higher orientation than the LLDPE when prepared under the same conditions. This would seem to be consistent with the lower melt index of the LDPE sample as shown in *Table 1*. The lower melt index would indicate a likelihood of higher melt stress during film blowing and resulting higher orientation (16). Also, the changes in orientation with processing conditions within the range studied were small. For all the samples the *c*-axis orientation factor lies near the altitude of the orientation triangle, indicating approximately equal biaxial orientation of the chains. The *a*-axis orientation factors always lie on or near the f_1^B axis, indicating that the *a*-axes are distributed in a nearly uniaxial manner about the *MD*. The *b*-axes have f_{1b}^B values which are near −0.5 indicating that the *b*-axes tend to be perpendicular to the *MD*. The fact that f_{2b}^B values are also negative indicates that there is a slight tendency for the *b*-axes to become perpendicular to the *TD*. This tendency is greater for the LDPE than the LLDPE.

These results may be compared with data previously published by Lindenmeyer and Lustig (8) and by Desper (9). Both authors show pole figures for LDPE blown films produced with certain blowing conditions that have very similar appearance to those of the LDPE and LLDPE samples investigated here. The tendency for *b*-axis orientation towards the film normal is perhaps a result of preferential nucleation at the surface of the film as discussed by Desper (9). The *a*-axis orientation along *MD* has often been observed in polyethylenes and has frequently been interpreted to result from a row nucleated structure (12, 13, 16, 23), although other interpretations are possible.

The amorphous orientation factors presented in *Table 4* show that negative values and chains in the amorphous region tend to be perpendicular to the film surface. One possible interpretation of these results is that the chains that are more highly oriented along *MD* (or *TD*) in the melt crystallize more readily during freezing. This produces crystals with their chain axes approximately parallel to either *MD* or *TD* and depletes the remaining amorphous material of chains having these orientations. This remaining amorphous material is left with chain orientations, which tend to be perpendicular to both *MD* and *TD*.

Surface Roughness and Optical Clarity

For all the samples examined, including the HDPE as well as the LDPE and LLDPE samples, the surface phase direct transmission factor, T_s, is lower than the bulk phase direct transmisson factor, T_B. This indicates that the overall direct transmission factor is controlled primarily by effects at or near the surface. Presumably the low values of T_s are due to light scattering from rough surfaces. This was further suggested by a strong correlation of surface phase direct transmission factor with the standard deviation of the height, σ, measured from the surface roughness profile. Previous investigators (2, 5, 24) have attributed the scattering from film surfaces to two different mechanisms: 1) crystallization-induced surface roughness, and 2) die-flow-induced surface roughness (the so-called extrusion haze). The former would be expected to vary with the level of crystallinity and the morphology of crystallization. The latter depends on extrusion conditions and would be expected to be a function of the rheological properties of the melt, which in turn depends on the molecular characteristics of the polymer.

For the present samples there are changes of both T_s and T_B with film processing variables. It would appear that the changes in T_s are associated with the changes in σ. The changes in T_B seem to be related largely to changes in the cooling rate of the films. For example, a decrease of overall direct transmission factor, T, with increasing frost-line height is due to a decrease of both the surface phase direct transmission factor, T_s, and the bulk phase direct transmission factor, T_B. As frost-line height increases, larger crystalline aggregates may be formed because of slower cooling rate. It is suggested that these larger crystalline aggregates produce more light scattering from the bulk phase, thus lower T_B. The larger crystalline aggregates at or near the film surface may also cause greater surface irregularities (larger σ) resulting in greater surface scattering and smaller T_s.

As drawdown ratio and blowup ratio increase, the bulk phase direct transmission factor increases and turbidity decreases. This would appear due to faster cooling rate and smaller crystalline aggregate size. In spite of this increase in T_B, the surface phase direct transmission factor, T_s, decreases with increasing drawdown and blowup ratios. This decrease of T_s must be associated with some kind of flow defects which cause surface roughness and not with the crystallization induced roughness. Huck and Clegg (2) suggested that extrusion defects should be smoothed out by drawing of the film, and hence light scattering due to extrusion defects should be reduced by increasing drawdown and blowup ratios. However, our result does not agree with this explanation. Howells and Benbow (24) suggested that extrusion defects may tend to disappear due to a relaxation process between the die and the frost-line. Lower drawdown ratios and slower cooling rates would tend to increase the effect of such a relaxation process. Our results seem to be more consistent with this explanation. Other hypotheses are possible. The surface roughness may in part be due to external disturbances "machine noise" and its interaction with the melt deformation processes in the film.

Since the total surface scattering results from a combination of the crystallization induced surface roughness and die and film-flow-induced surface roughness, it is not always clear which contribution predominates.

The observation by SEM of features which appear to be associated with a row nucleated crystalline morphology together with their high crystallinity suggests that the high surface scattering (small T_s) of the HDPE samples is largely associated with crystallization-induced surface roughness. The layered features one observes, however, might not be from this mechanism. They however do parallel the 100 Å unit lamellae structures found in transmission electron microscopy. The effect of crystallization on the surface roughness is much smaller for the LDPE and LLDPE samples. The crystallization-induced roughness appears to be about the same order or smaller than the flow-induced surface roughness in the LDPE and LLDPE samples. This is based on the fact that the changes in transmission with drawdown and blowup ratios must be ascribed to effects due to flow defects. It does not appear feasible to further separate these effects based on the present data.

CONCLUSIONS

In summary, the majority of light scattered from LDPE, LLDPE, and HDPE films was from the surface and not from the film interior. The transmission coefficient for the surface contribution decreased monotonically as surface roughness, measured by the standard deviation of the surface height, increased. Variations in light scattering due to the surface roughness and bulk phase irregularities occur due to changes in film process conditions. These effects were discussed in terms of changes in crystalline morphology and surface roughness produced by flow defects generated during extrusion and in the film, but it was not feasible to reach definite conclusions regarding the relative importance of these mechanisms for the present LDPE and LLDPE samples.

REFERENCES

1. A. C. Webber, *J. Opt. Soc. America*, **47**, 785 (1957).
2. N. C. Huck and P. L. Clegg, *SPE Trans.*, **1**, 121 (1961).
3. V. G. Kendall, *Trans. Plastics Inst.*, **31**, 49 (1963).
4. T. Hashimoto, A. Todd, Y. Murakami, and H. Kawai, *J. Polym. Sci. Polym. Phys.* Ed., **15**, 501 (1977).
5. F. C. Stehling, C. S. Speed, and L. Westerman, *Macromolecules*, **14**, 698 (1981).
6. B. H. Clampitt, D. E. German, and H. D. Anspon, *Anal. Chem.*, **41**, 1306 (1969).
7. D. R. Holmes and R. P. Palmer, *J. Polym. Sci.*, **31**, 345 (1958).
8. P. H. Lindenmeyer and S. Lustig, *J. Appl. Polym. Sci.*, **9**, 227 (1965).
9. C. R. Desper, *J. Appl. Polym. Sci.*, **13**, 169 (1969).
10. T. Nagasawa, T. Matsumura, S. Hoshino, and K. Kobayoshi, *Appl. Polym. Symp.*, **20**, 275 (1973).
11. T. Nagasawa, T. Matsumura, and S. Hoshino, *Appl. Polym. Symp.*, **20**, 295 (1973).
12. W. F. Maddams and J. E. Preedy, *J. Appl. Polym. Sci.*, **22**, 2721 (1978).
13. W. F. Maddams and J. E. Preedy, *J. Appl. Polym. Sci.*, **22**, 2739 (1978).
14. W. F. Maddams and J. E. Preedy, *J. Appl. Polym. Sci.*, **22**, 2751 (1978).
15. K. J. Choi, J. L. White, and J. E. Spruiell, *J. Appl. Polym. Sci.*, **25**, 2777 (1980).
16. K. J. Choi, J. E. Spruiell, and J. L. White, *J. Polym. Sci. Polym. Phys. Ed.*, **20**, 27 (1982).
17. Y. Shimomura, J. E. Spruiell, and J. L. White, *J. Appl. Polym. Sci.*, **27**, 2663 (1982).
18. Y. Shimomura, J. E. Spruiell, and J. L. White, *Polym. Eng. Rev.*, **2**, 417 (1983).
19. J. L. White and J. E. Spruiell, *Polym. Eng. Sci.*, **23**, 247 (1983).
20. J. L. White and J. E. Spruiell, *Polym. Eng. Sci.*, **21**, 859 (1981).
21. R. S. Stein, *J. Polym. Sci.*, **31**, 335 (1958).
22. R. S. Stein, *J. Polym. Sci.*, **24**, 383 (1957).
23. A. Keller and M. J. Machin, *J. Macromol. Sci. Phys.*, **B1**, 41 (1967).
24. E. R. Howells and J. J. Benbow, *Trans. J. Plast. Inst.*, **30**, 240 (1962).